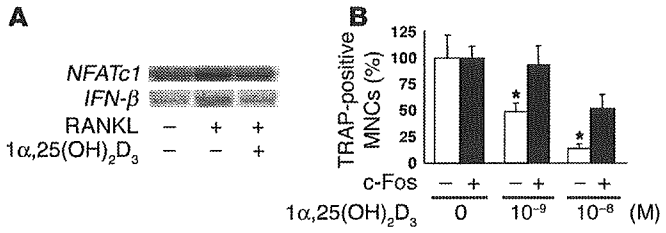

Figure 7
c-Fos protein as a target of anti-osteoclastogenic action of $1\alpha,25(OH)_2D_3$. Osteoclast precursor cells were isolated from the bone marrow of C57BL/6J mice as M-CSF–dependent adherent cells and were treated with RANKL (40 ng/ml) for 24 hours in the absence or presence of the indicated doses of $1\alpha,25(OH)_2D_3$. (**A**) Northern blot analysis of c-Fos target genes, i.e., *NFATc1* and *IFN-β*, in RANKL-treated osteoclast precursor cells without or with $1\alpha,25(OH)_2D_3$ for 24 hours (10^{-7} M). (**B**) Forced expression of c-Fos (indicated by "+") by a retroviral vector abrogated the suppressive effect of $1\alpha,25(OH)_2D_3$ on osteoclast development. Osteoclast precursor cells isolated from bone marrow were infected with a retroviral vector encoding c-Fos, and cultured with M-CSF and RANKL for 3 days in the absence or presence of $1\alpha,25(OH)_2D_3$. Data are expressed as a percentage of the value for vehicle-treated cultures without retroviral infection (–). $^*P < 0.05$ versus vector-infected group, $n = 6$.

min D, has been controversial (25, 26). It is generally believed that $1\alpha,25(OH)_2D_3$ stimulates bone resorption, based on the fact that it was found to be a bone-resorbing hormone in a classic experiment using bone organ cultures (27), and the fact that $1\alpha,25(OH)_2D_3$ induces the expression of RANKL, an essential cytokine for osteoclast development (28). In the present study we have provided biochemical as well as histological evidence that vitamin D hormone can exert a pharmacological action to inhibit bone resorption under pathological conditions with excessive osteoclast generation. The exact reason for these contrasting effects of $1\alpha,25(OH)_2D_3$ on bone resorption is not clear at the present time. $1\alpha,25(OH)_2D_3$ at high concentrations is known to induce the expression of RANKL in stromal/osteoblastic cells in vitro, which is assumed to favor osteoclastogenesis. In sharp contrast, as demonstrated in the current study, $1\alpha,25(OH)_2D_3$ can act on hematopoietic lineage cells and potently inhibit their differentiation into mature osteoclasts. $1\alpha,25(OH)_2D_3$ has also been shown to inhibit osteoclast differentiation from human PBMCs (29). We (7, 8, 30) and others (31) have previously reported that when vitamin D hormone is administered in vivo at pharmacological doses in animal models with excessive bone resorption, it actually reduces osteoclast number and suppresses bone resorption. This has been proven in a recent clinical trial, in which ED-71, a vitamin D analog, reduced a bone resorption marker and increased BMD in osteoporotic patients with native vitamin D_3 supplementation (32). It is conceivable, therefore, that in vivo, the anti-osteoclastogenic action through VDR in hematopoietic cells may outweigh the pro-osteoclastogenic action through stromal cells, leading to a net decrease in bone resorption. In fact, we failed to find an increase in RANKL expression in vivo even when toxic doses of $1\alpha,25(OH)_2D_3$ that induced overt hypercalcemia were administered (9). Others have reported that $1\alpha,25(OH)_2D_3$ within a certain dose range inhibits parathyroid hormone–induced (PTH-induced) RANKL expression in the bones of thyroparathyroidectomized rats (31). Alternatively, under pathological conditions with elevated bone resorption, VDR signaling may be downregulated in stromal/osteoblastic cells, relative to that in hematopoietic cells, which would mask the pro-osteoclastogenic action of vitamin D. Further studies are required to determine the relative contribution of stromal versus hematopoietic cells to the in vivo regulation of bone resorption through the VDR.

The major action of vitamin D is stimulation of intestinal calcium absorption; and the therapeutic effects of vitamin D on bone, whether active or plain vitamin D, are believed to be indirect, through stimulation of intestinal calcium absorption, correction of a negative calcium balance, and normalization of the sustained PTH secretion frequently seen in elderly patients (33). In order to gain some insight into the role of PTH suppression in vitamin D action on bone, we previously examined the effects of $1\alpha,25(OH)_2D_3$ and its analog [22-oxa-$1\alpha,25(OH)_2D_3$] on bone resorption in parathyroidectomized rats rendered hypercalcemic with constant PTH-related protein infusion (34). Under these "PTH clamp" conditions, we observed that $1\alpha,25(OH)_2D_3$ and 22-oxa-1α,25-dihydroxyvitamin D_3 were capable of inhibiting bone resorption (34). In agreement with these previous findings, we have demonstrated in this study that vitamin D hormone acts directly on hematopoietic cells in bone marrow, through VDR expressed in osteoclast progenitors of the monocyte/macrophage lineage, thereby inhibiting their terminal differentiation into mature osteoclasts. Thus, hematopoietic cells that receive the RANKL signal through the RANK receptor are important target cells of vitamin D action in vivo.

We further investigated the mechanism by which $1\alpha,25(OH)_2D_3$ modulates the developmental program of hematopoietic precursor cells and inhibits their differentiation into mature osteoclasts. This process is tightly regulated by extracellular signals, including RANKL as an essential cytokine, as well as by negative regulators, such as OPG and other inhibitory molecules (35, 36). Our find-

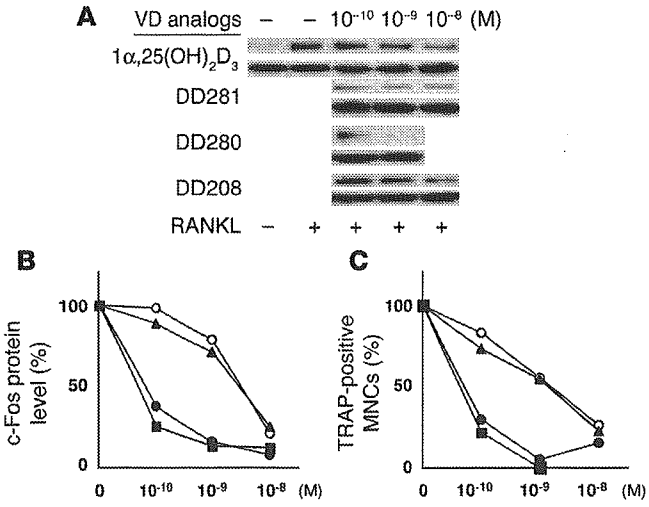

Figure 8
Screening for vitamin D (VD) analogs that reduce c-Fos protein and inhibit osteoclast differentiation more potently than $1\alpha,25(OH)_2D_3$. The effects of $1\alpha,25(OH)_2D_3$ (open circles) and its analogs (DD281, DD280, and DD208) on the c-Fos protein level in osteoclast precursor cells (**A** and **B**) and the formation of TRAP-positive multinucleate osteoclasts (**C**) at the indicated concentrations are shown. The lower bands in **A** show β-actin as an internal control for protein loading. Filled circles, rectangles, and triangles (**B** and **C**) represent DD281, DD280, and DD208, respectively. Data are expressed as a percentage of the value for vehicle-treated cultures.

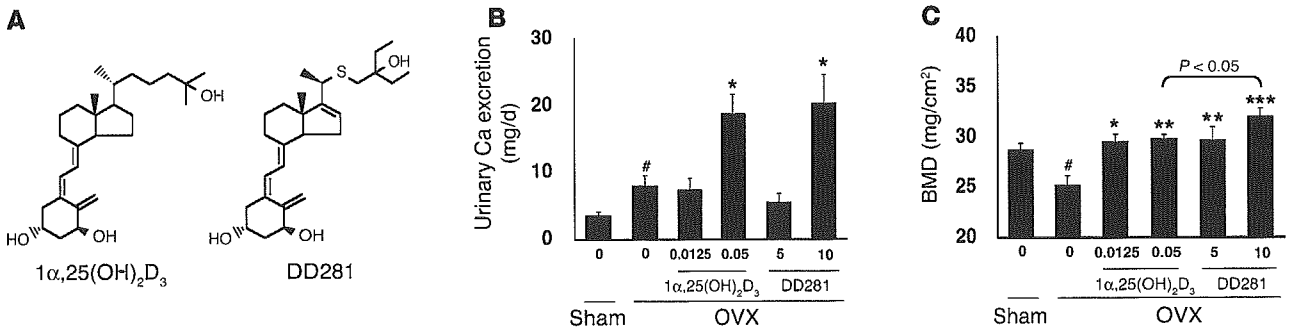

Figure 9
A novel vitamin D analog, DD281, inhibits osteoclast differentiation and increases BMD more potently than $1\alpha,25(OH)_2D_3$ in vivo. (**A**) Structures of $1\alpha,25(OH)_2D_3$ and its analog, DD281. (**B**) Ovariectomized (OVX) C57BL/6J mice were treated orally with the indicated doses of $1\alpha,25(OH)_2D_3$ or its analog DD281 for 4 weeks, and urinary calcium excretion was determined for the final 24 hours. $^*P < 0.05$ versus OVX group with vehicle treatment, $^{\#}P < 0.05$ versus sham group, $n = 8$ each group. (**C**) BMD at the lumbar vertebrae was determined. $^*P < 0.05$ versus OVX group with vehicle treatment, $^{**}P < 0.005$ versus OVX group with vehicle treatment, $^{***}P < 0.0005$ versus OVX group with vehicle treatment, $^{\#}P < 0.05$ versus sham group, $n = 8$ each group.

ings that $1\alpha,25(OH)_2D_3$ inhibited bone resorption in mice lacking OPG rule out the possibility that the antiresorptive action is mediated through OPG. It is also unlikely that $1\alpha,25(OH)_2D_3$ interferes with the binding of RANKL to its receptor RANK and inhibits its overall signaling, since some intracellular signals activated downstream of RANK, such as IκB kinase and JNK, were not affected by $1\alpha,25(OH)_2D_3$. Instead, our data suggest that, among known signaling molecules involved in osteoclast development downstream of the RANK receptor, c-Fos protein is a key target molecule of VDR. In addition, our experiments revealed that the reduction in the level of c-Fos protein took place with only a modest decrease in its mRNA level. Taken together with the results of the pulse-labeling experiments, this finding suggests that VDR, classically viewed as a transcription factor, inhibits the translation of c-Fos protein, although the underlying molecular mechanism remains elusive. The effect of $1\alpha,25(OH)_2D_3$ on c-Fos protein in osteoclast precursors contrasts with the reported effect of $1\alpha,25(OH)_2D_3$ on c-Fos gene transcription in osteoblasts and other cell types (37, 38). Thus, there may exist cell type–specific regulatory mechanisms that modulate the expression of c-Fos gene expression in response to $1\alpha,25(OH)_2D_3$. Since a number of other proteins involved in RANK signaling, such as RANK itself, JNK, p38 MAPK, IκB kinase, p65 and p52 subunits of NF-κB, and c-Jun, were not affected by $1\alpha,25(OH)_2D_3$, it is conceivable that the inhibitory effect of the VDR is specific to c-Fos protein in osteoclast precursor cells.

Importantly, the suppression of c-Fos protein through VDRs is critical for the pharmacological action of vitamin D, since we showed that forced expression of c-Fos blocked the suppressive effect of vitamin D on osteoclast formation. The identification of novel synthetic vitamin D analogs that were capable of inhibiting osteoclast development more efficiently than the natural hormone, $1\alpha,25(OH)_2D_3$, in parallel with greater suppression of c-Fos protein, lends further support to our concept that c-Fos–suppressing activity is important for the antiresorptive function of vitamin D. This mechanism may also underlie the activity of other recently developed bone-selective vitamin D analogs (39, 40). It should be noted, however, that DD281 was not completely bone-selective and increased urinary calcium excretion above that in the vehicle-treated mice. Therefore, careful monitoring of urinary and serum calcium levels would be required if its clinical utility were to be tested.

In conclusion, we demonstrated herein that the pharmacological action of $1\alpha,25(OH)_2D_3$ is to mitigate excessive bone resorption, under pathological conditions such as osteoporosis; that it does so by acting on monocyte/macrophage-lineage cells in bone marrow; that the presence of VDRs is a prerequisite for this action; and that c-Fos protein is a key target molecule of VDR action. Based on these findings, we synthesized new vitamin D analogs, among which DD281, with potent antiresorptive activity relative to calcium absorption function, may warrant clinical trial for the treatment of bone diseases associated with excessive osteoclastic activity.

Methods

Reagents. $1\alpha,25(OH)_2D_3$ and its analogs, including DD208, DD280, and DD281, were synthesized at Chugai Pharmaceutical Co. Mouse RANKL and M-CSF were purchased from R&D Systems. Antibodies against RANK, TRAF6, p65, and p52 were purchased from Santa Cruz Biotechnology Inc. Anti-c-Jun and -c-Fos antibodies came from Sigma-Aldrich.

Animal experiments. Six-week-old female *OPG* homozygous and heterozygous KO mice were purchased from CLEA Japan Inc. and acclimated for 1 week under standard laboratory conditions at 24 ± 2°C and

Table 1
Effects of $1\alpha,25(OH)_2D_3$ and DD281 on osteoclast parameters in OVX mice

Treatment		$1\alpha,25(OH)_2D_3$		DD281	
Dose (μg/kg body weight)	0	0.0125	0.05	5	10
Oc.S/BS (%)	13.3 ± 0.7	10.5 ± 1.4	11.1 ± 0.4[A]	11.3 ± 0.8	9.8 ± 0.4[B,C]
N.Oc/BS (no./mm)	2.5 ± 0.2	2.2 ± 0.3	2.4 ± 0.2	2.3 ± 0.2	1.8 ± 0.2[A,C]

Eleven-week-old OVX mice ($n = 8$ each group) were treated with $1\alpha,25(OH)_2D_3$ or DD281 at the indicated doses for 4 weeks. Bone histomorphometry was performed at the lumbar spine. Oc.S/BS, bone surface covered by osteoclasts; N.Oc/BS, number of osteoclasts, corrected for bone surface. $^AP < 0.05$ versus OVX group, $^BP < 0.005$ versus OVX group, $^CP < 0.05$ versus $1\alpha,25(OH)_2D_3$-treated group.

Table 2
Blood and urine biochemistry in OVX mice treated with $1\alpha,25(OH)_2D_3$ or DD281

Operation	Sham	OVX				
Treatment	Vehicle	Vehicle	$1\alpha,25(OH)_2D_3$		DD281	
Dose (μg/kg body weight)			0.0125	0.05	5	10
Serum						
Calcium (mg/dl)	9.63 ± 0.13	9.34 ± 0.11	9.09 ± 0.09	9.69 ± 0.09[A]	9.19 ± 0.05	9.31 ± 0.11
Phosphorus (mg/dl)	8.35 ± 0.39	7.50 ± 0.41	6.36 ± 0.24[A]	8.19 ± 0.47	6.39 ± 0.21	7.23 ± 0.19
Urine						
Phosphorus/Creatinine	6.71 ± 0.45	6.74 ± 0.44	7.75 ± 0.32	7.10 ± 0.52	6.28 ± 0.56	6.32 ± 0.32

Eleven-week-old OVX mice ($n = 8$ per group) were treated with $1\alpha,25(OH)_2D_3$ or DD281 at the indicated doses for 4 weeks. Urine was collected during the final 24 hours, and blood was drawn to obtain serum. [A]$P < 0.05$ versus OVX group.

50–60% humidity. The mice were allowed free access to tap water and commercial standard rodent chow (CE-2) containing 1.20% calcium, 1.08% phosphate, and 240 IU/100 g vitamin D_3 (CLEA Japan Inc.). After acclimation, various doses of $1\alpha,25(OH)_2D_3$ or vehicle (medium chain triglyceride) were administered orally 5 times a week for 6 weeks.

Nine-week-old female C57BL/6J mice were purchased from Japan SLC Inc. and ovariectomized (OVX) after a 1-week acclimation. Sham-operated mice served as the control. OVX mice were treated orally with $1\alpha,25(OH)_2D_3$ (0.0125–0.05 μg/kg body weight once daily), its analog DD281 (5–10 μg/kg body weight twice daily), or vehicle (medium chain triglyceride) 5 times a week for 4 weeks. Urine was collected during the final 24 hours, and blood samples were centrifuged to obtain the serum.

All experiments were performed in accordance with Chugai Pharmaceutical Co.'s ethical guidelines for animal care, and the experimental protocols were approved by the animal care committee of the company and by the Animal Experimentation Ethics Committee of the National Center for Geriatrics and Gerontology.

Bone analysis. For bone analysis, right femurs and lumbar vertebrae were dissected and stored in 70% ethanol. BMD was measured by dual-energy x-ray absorptiometry (DCS-600EX; ALOKA Inc.). Left femurs and lumbar vertebrae were fixed in 4% paraformaldehyde for bone histomorphometry as described previously (7, 8). Each sample was sectioned, and then stained for tartrate-resistant acid phosphatase (TRAP). Histomorphometric parameters were measured at Niigata Bone Science Institute (Niigata, Japan).

Biochemical analysis. Serum and urinary calcium concentrations were determined using an autoanalyzer (Hitachi 7170). Urinary deoxypyridinoline was measured with a PYRILINKS-D assay kit (Metra Biosystems Inc.).

Osteoclastogenesis assay in vitro. Bone marrow cells were isolated from the tibiae and femurs of 6- to 9-week-old male C57BL/6J mice (SLC) and *VDR* KO mice (kindly provided by Shigeaki Kato, University of Tokyo, Tokyo, Japan). All cells were plated in culture dishes containing α-MEM/10% heat-inactivated FBS/1% antibiotics and incubated for 12 hours. Nonadherent cells were separated and cultured for 3 days with M-CSF (30 ng/ml), and then those that became adherent were used as osteoclast precursor cells. Cells were treated with RANKL (40 ng/ml) in the absence or presence of $1\alpha,25(OH)_2D_3$ for 3 days, fixed in 4% paraformaldehyde, and stained for TRAP. Multinucleate (≥3 nuclei), TRAP-positive cells were counted as osteoclasts. Osteoclast precursor cells were cultured in the presence of 30 ng/ml M-CSF without or with increasing doses of $1\alpha,25(OH)_2D_3$ for 3 days, and cell proliferation was assessed using a Cell Counting Kit-8 (Dojindo Laboratories).

Western and Northern analyses. Whole-cell extracts were isolated from osteoclast precursors, and protein concentrations were determined by use of a Bio-Rad Protein Assay kit (Bio-Rad Laboratories). Equivalent amounts of protein were loaded for 4–20% SDS-PAGE, and proteins transferred onto the membrane were detected with an ECL Plus Western blotting detection system (Amersham Biosciences). Phosphorylation of JNK, p38 MAPK, and IκB kinase was evaluated using kits from Cell Signaling Technology. Total RNA was isolated with TRIzol reagent (Invitrogen Corp.), according to the manufacturer's instructions. For Northern analysis, equal amounts of total RNA (10 μg/lane) were fractionated on a 1.5% agarose gel. The specific mRNAs were detected by hybridization of Hybond N^+ nylon membranes (Amersham Biosciences) with ^{32}P-labeled cDNA probes for mouse c-Fos, IFN-β, and NFATc1. For quantitative RT-PCR, total RNA (1 μg) was reverse transcribed using SuperScript III (Invitrogen Corp.), and samples were analyzed using a LightCycler (Roche Diagnostics Corp.). The primers included 5′-ACCTGTTCGTGAAACACACCA-3′ and 5′-ACAACACACTCCATGCGGTTT-3′ for c-Fos, 5′-GGACATTGGCATGATGAAGG-3′ and 5′-CTCAGACTGTCCTTCAAGGC-3′ for VDR, and 5′-TGCTGCCATTGTTGATATGG-3′ and 5′-TCCACAGCTTTGATGACACC-3′ for EF-1α. The amount of c-Fos and VDR mRNA was corrected by that of EF-1α mRNA.

Pulse-labeling and pulse-chase labeling experiments. For pulse labeling, osteoclast precursor cells were stimulated with RANKL for 24 hours in the absence or presence of $1\alpha,25(OH)_2D_3$ at 10^{-7} M and then radiolabeled for 1 hour with culture medium containing 150 μCi/ml of a ^{35}S-methionine and cysteine mixture (Amersham Biosciences). In the case of pulse-chase labeling, RANKL-treated osteoclast precursors were similarly radiolabeled and then incubated in the presence of nonradioactive medium containing 10 mM cold methionine and 10 mM cold cysteine for various periods of time. Cell extracts were immunoprecipitated with anti–c-Fos antibody, and the precipitates were then subjected to SDS-PAGE. After the gels had been dried, autoradiography was performed.

Retroviral expression of c-Fos protein. A retroviral vector encoding mouse c-Fos (pBabe-cFos, kindly provided by K. Matsuo, Keio University, Tokyo, Japan) was used to transfect Plat-E retrovirus packaging cells (a gift from T. Kitamura, University of Tokyo, Tokyo, Japan). The culture media were collected 48 hours after the transfection and kept as retrovirus stocks. Osteoclast precursor cells were exposed to the retrovirus in the presence of polybrene (8 μg/ml) for 1 day and were subsequently treated with RANKL and $1\alpha,25(OH)_2D_3$ for 4 days in the presence of puromycin (1.6 μg/ml). Osteoclast differentiation was evaluated as described above.

Statistics. Data were expressed as the means ± SEM. Statistical analysis was carried out by ANOVA, using Statistical Analysis System software (SAS Institute Inc.). The significance of differences was determined using 2-tailed Student's t test and Dunnett's multiple test. A value of $P < 0.05$ was considered to indicate a significant difference.

Acknowledgments

We thank Shigeaki Kato and Toshio Kitamura (University of Tokyo) for providing VDR KO mice and retroviral vectors, respectively; Koichi Matsuo, Sunao Takeshita, and Ken Watanabe (National Center for Geriatrics and Gerontology) for valuable suggestions; Mie Suzuki (National Center for Geriatrics and Gerontology) for expert technical assistance; and Akemi Ito (Niigata Bone Science Institute) for discussion on the data of bone histomorphometry. This study was supported in part by grants from the program Comparative Research on Aging and Health of the Ministry of Health, Labor, and Welfare of Japan (to K. Ikeda) and by a grant from the Program for Promotion of Fundamental Studies in Health Sciences of the National Institute of Biomedical Innovation of Japan (MF-14 to K. Ikeda).

Received for publication February 14, 2005, and accepted in revised form November 8, 2005.

Address correspondence to: Kyoji Ikeda, Department of Bone and Joint Disease, Research Institute, National Center for Geriatrics and Gerontology, 36-3 Gengo, Morioka, Obu, Aichi 474-8522, Japan. Phone and Fax: 81-562-46-8094; E-mail: kikeda@nils.go.jp.

1. Cummings, S.R., and Melton, L.J. 2002. Epidemiology and outcomes of osteoporotic fractures. *Lancet.* **359**:1761–1767.
2. Teitelbaum, S.L. 2000. Bone resorption by osteoclasts. *Science.* **289**:1504–1508.
3. Suda, T., et al. 1999. Modulation of osteoclast differentiation and function by the new members of the tumor necrosis factor receptor and ligand families. *Endocr. Rev.* **20**:345–357.
4. Karsenty, G., and Wagner, E.F. 2002. Reaching a genetic and molecular understanding of skeletal development. *Dev. Cell.* **2**:389–406.
5. Parfitt, A.M., et al. 1996. A new model for the regulation of bone resorption, with particular reference to the effects of bisphosphonates. *J. Bone Miner. Res.* **11**:150–159.
6. Rodan, G.A., and Martin, T.J. 2000. Therapeutic approaches to bone diseases. *Science.* **289**:1508–1514.
7. Shiraishi, A., et al. 2000. Alfacalcidol inhibits bone resorption and stimulates formation in an ovariectomized rat model of osteoporosis: distinct actions from estrogen. *J. Bone Miner. Res.* **15**:770–779.
8. Uchiyama, Y., et al. 2002. ED-71, a vitamin D analog, is a more potent inhibitor of bone resorption than alfacalcidol in an estrogen-deficient rat model of osteoporosis. *Bone.* **30**:582–588.
9. Shibata, T., et al. 2002. Vitamin D hormone inhibits osteoclastogenesis in vivo by decreasing the pool of osteoclast precursors in bone marrow. *J. Bone Miner. Res.* **17**:622–629.
10. Manolagas, S.C., and Jilka, R.L. 1995. Bone marrow, cytokines, and bone remodeling. Emerging insights into the pathophysiology of osteoporosis. *N. Engl. J. Med.* **332**:305–311.
11. Pacifici, R. 1996. Estrogen, cytokines, and pathogenesis of postmenopausal osteoporosis. *J. Bone Miner. Res.* **11**:1043–1051.
12. Shevde, N.K., Bendixen, A.C., Dienger, K.M., and Pike, J.W. 2000. Estrogens suppress RANK ligand-induced osteoclast differentiation via a stromal cell independent mechanism involving c-Jun repression. *Proc. Natl. Acad. Sci. U. S. A.* **97**:7829–7834.
13. Simonet, W.S., et al. 1997. Osteoprotegerin: a novel secreted protein involved in the regulation of bone density. *Cell.* **89**:309–319.
14. Bucay, N., et al. 1998. Osteoprotegerin-deficient mice develop early onset osteoporosis and arterial calcification. *Genes Dev.* **12**:1260–1268.
15. Reichel, H., Koeffler, H.P., and Norman, A.W. 1989. The role of the vitamin D endocrine system in health and disease. *N. Engl. J. Med.* **320**:980–991.
16. Ferrara, P., et al. 2003. The structural determinants responsible for c-Fos protein proteasomal degradation differ according to the conditions of expression. *Oncogene.* **22**:1461–1474.
17. Grigoriadis, A.E., et al. 1994. c-Fos: a key regulator of osteoclast-macrophage lineage determination and bone remodeling. *Science.* **266**:443–448.
18. Matsuo, K., et al. 2000. Fosl1 is a transcriptional target of c-Fos during osteoclast differentiation. *Nat. Genet.* **24**:184–187.
19. Takayanagi, H., et al. 2002. Induction and activation of the transcription factor NFATc1 (NFAT2) integrate RANKL signaling in terminal differentiation of osteoclasts. *Dev. Cell.* **3**:889–901.
20. Takayanagi, H., et al. 2002. RANKL maintains bone homeostasis through c-Fos-dependent induction of interferon-beta. *Nature.* **416**:744–749.
21. Matsuo, K., et al. 2004. Nuclear factor of activated T-cells (NFAT) rescues osteoclastogenesis in precursors lacking c-Fos. *J. Biol. Chem.* **279**:26475–26480.
22. Yoshizawa, T., et al. 1997. Mice lacking the vitamin D receptor exhibit impaired bone formation, uterine hypoplasia and growth retardation after weaning. *Nat. Genet.* **16**:391–396.
23. Thomas, M.K., et al. 1998. Hypovitaminosis D in medical inpatients. *N. Engl. J. Med.* **338**:777–783.
24. Trivedi, D.P., Doll, R., and Khaw, K.T. 2003. Effect of four monthly oral vitamin D3 (cholecalciferol) supplementation on fractures and mortality in men and women living in the community: randomised double blind controlled trial. *BMJ.* **326**:469–475.
25. Hauselmann, H.J., and Rizzoli, R. 2003. A comprehensive review of treatments for postmenopausal osteoporosis. *Osteoporos. Int.* **14**:2–12.
26. Papadimitropoulos, E., et al. 2002. Meta-analyses of therapies for postmenopausal osteoporosis. VIII. Meta-analysis of the efficacy of vitamin D treatment in preventing osteoporosis in postmenopausal women. *Endocr. Rev.* **23**:560–569.
27. Raisz, L.G., Trummel, C.L., Holick, M.F., and DeLuca, H.F. 1972. 1,25-Dihydroxycholecalciferol: a potent stimulator of bone resorption in tissue culture. *Science.* **175**:768–769.
28. Yasuda, H., et al. 1998. Osteoclast differentiation factor is a ligand for osteoprotegerin/osteoclastogenesis-inhibitory factor and is identical to TRANCE/RANKL. *Proc. Natl. Acad. Sci. U. S. A.* **95**:3597–3602.
29. Itonaga, I., Sabokbar, A., Neale, S.D., and Athanasou, N.A. 1999. 1,25-Dihydroxyvitamin D(3) and prostaglandin E(2) act directly on circulating human osteoclast precursors. *Biochem. Biophys. Res. Commun.* **264**:590–595.
30. Shiraishi, A., et al. 1999. The advantage of alfacalcidol over vitamin D in the treatment of osteoporosis. *Calcif. Tissue Int.* **65**:311–316.
31. Ueno, Y., et al. 2003. In vivo administration of 1,25-dihydroxyvitamin D3 suppresses the expression of RANKL mRNA in bone of thyroparathyroidectomized rats constantly infused with PTH. *J. Cell. Biochem.* **90**:267–277.
32. Matsumoto, T., et al. 2005. A new active vitamin D, ED-71, increases bone mass in osteoporotic patients under vitamin D supplementation: a randomized, double-blind, placebo-controlled clinical trial. *J. Clin. Endocrinol. Metab.* **90**:5031–5036.
33. Lips, P. 2001. Vitamin D deficiency and secondary hyperparathyroidism in the elderly: consequences for bone loss and fractures and therapeutic implications. *Endocr. Rev.* **22**:477–501.
34. Endo, K., et al. 2000. 1,25-Dihydroxyvitamin D3 as well as its analogue OCT lower blood calcium through inhibition of bone resorption in hypercalcemic rats with continuous parathyroid hormone-related peptide infusion. *J. Bone Miner. Res.* **15**:175–181.
35. Choi, S.J., et al. 1999. Identification of human asparaginyl endopeptidase (legumain) as an inhibitor of osteoclast formation and bone resorption. *J. Biol. Chem.* **274**:27747–27753.
36. Zhou, H., et al. 2001. A novel osteoblast-derived C-type lectin that inhibits osteoclast formation. *J. Biol. Chem.* **276**:14916–14923.
37. Schrader, M., Kahlen, J.P., and Carlberg, C. 1997. Functional characterization of a novel type of 1 alpha,25-dihydroxyvitamin D3 response element identified in the mouse c-fos promoter. *Biochem. Biophys. Res. Commun.* **230**:646–651.
38. Candeliere, G.A., Prud'homme, J., and St-Arnaud, R. 1991. Differential stimulation of fos and jun family members by calcitriol in osteoblastic cells. *Mol. Endocrinol.* **5**:1780–1788.
39. Shevde, N.K., et al. 2002. A potent analog of 1alpha,25-dihydroxyvitamin D3 selectively induces bone formation. *Proc. Natl. Acad. Sci. U. S. A.* **99**:13487–13491.
40. Peleg, S., Uskokovic, M., Ahene, A., Vickery, B., and Avnur, Z. 2002. Cellular and molecular events associated with the bone-protecting activity of the noncalcemic vitamin D analog Ro-26-9228 in osteopenic rats. *Endocrinology.* **143**:1625–1636.

The EMBO Journal (2006) 25, 554–564 | © 2006 European Molecular Biology Organization | All Rights Reserved 0261-4189/06
www.embojournal.org

THE EMBO JOURNAL

A novel ubiquitin-binding protein ZNF216 functioning in muscle atrophy

Akinori Hishiya[1,2], Shun-ichiro Iemura[3], Tohru Natsume[3], Shinichi Takayama[2], Kyoji Ikeda[1] and Ken Watanabe[1,*]

[1]Department of Bone & Joint Disease, National Center for Geriatrics & Gerontology (NCGG), Obu, Aichi, Japan, [2]Program of Molecular Chaperone Biology, Department of Radiology, Medical College of Georgia, Augusta, GA, USA and [3]Japan Biological Information Research Center (JBIRC), National Institute of Advanced Industrial Science & Technology (AIST), Tokyo, Japan

The ubiquitin–proteasome system (UPS) is critical for specific degradation of cellular proteins and plays a pivotal role on protein breakdown in muscle atrophy. Here, we show that ZNF216 directly binds polyubiquitin chains through its N-terminal A20-type zinc-finger domain and associates with the 26S proteasome. ZNF216 was colocalized with the aggresome, which contains ubiquitinylated proteins and other UPS components. Expression of *Znf216* was increased in both denervation- and fasting-induced muscle atrophy and upregulated by expression of constitutively active FOXO, a master regulator of muscle atrophy. Mice deficient in *Znf216* exhibited resistance to denervation-induced atrophy, and ubiquitinylated proteins markedly accumulated in neurectomized muscle compared to wild-type mice. These data suggest that ZNF216 functions in protein degradation via the UPS and plays a crucial role in muscle atrophy.

The EMBO Journal (2006) **25,** 554–564. doi:10.1038/sj.emboj.7600945; Published online 19 January 2006
Subject Categories: proteins; molecular biology of disease
Keywords: aggresome; muscular atrophy; proteasome; ubiquitin; zinc-finger protein

Introduction

The ubiquitin–proteasome system (UPS) is one of the major protein degradation pathways in eukaryotic cells. The UPS plays key regulatory roles in many cellular processes, including cell cycle control, the regulation of transcription and protein quality control (Hershko and Ciechanover, 1998; Pickart and Cohen, 2004). Aberrations of this system lead to many forms of pathogenesis, such as malignancies, neurodegenerative disease and inflammatory response (Glickman and Ciechanover, 2002). The UPS includes sequential, multistep reactions: ubiquitin-conjugation of target proteins by E1, E2 and E3 enzymes, recognition of ubiquitinylated proteins by ubiquitin-binding proteins or 19S subunits of proteasome and proteolysis in the proteasome.

Many catabolic conditions, such as low-insulin state, hyperthyroidism, sepsis and cancer cachexia lead to enhancement of protein breakdown in skeletal muscle known as muscle atrophy (Mitch and Goldberg, 1996; Lecker *et al*, 1999). In muscle atrophy, the UPS plays a pivotal role in protein breakdown (Price *et al*, 1996; Tawa *et al*, 1997). Several studies indicate that mRNAs encoding UPS components are increased in atrophying muscle (Medina *et al*, 1991; Wing and Goldberg, 1993; Bailey *et al*, 1996; Price *et al*, 1996; Jagoe *et al*, 2002). In particular, the E3 ubiquitin ligases MAFbx/Atrogin-1 and MuRF-1 (muscle RING finger 1) are known to be markers of muscle atrophy (Bodine *et al*, 2001; Gomes *et al*, 2001). Both are induced in multiple models of muscle atrophy including immobilization, denervation and hindlimb suspension, and mice deficient in either gene are resistant to denervation-induced muscle atrophy (Bodine *et al*, 2001). Goldberg and co-workers proposed that atrophy-related genes, whose expression is induced in multiple types of muscle atrophy, are called 'atrogenes' (Sandri *et al*, 2004). Recently, it was demonstrated that the IGF-I/PI3K/Akt pathway is an important regulator of muscle mass in muscle hypertrophy and atrophy (Sacheck *et al*, 2004; Sandri *et al*, 2004; Stitt *et al*, 2004). In that case, the transcription factor FOXO plays a pivotal role in activating atrogenes such as MAFbx/Atrogin-1 (Gomes *et al*, 2001).

Although many UPS players such as E3 ligases have been characterized, the mechanism of how ubiquitinylated proteins are delivered to the proteasome have not been fully elucidated. A component of 19S proteasome, Rpn10/S5a, recognizes the ubiquitinylated proteins (Young *et al*, 1998; Wilkinson *et al*, 2000). It has been shown that yeast proteins, Rad23p and Dsk2p, bind to ubiquitinylated substrates and to the 26S proteasome through their UBA and Ubl domains, respectively, thereby functioning as shuttle proteins that present polyubiquitinylated proteins to the proteasome (Chen *et al*, 2001; Funakoshi *et al*, 2002; Elsasser and Finley, 2005). Loss-of-function of shuttle proteins results in abnormal accumulation of polyubiquitinylated proteins (Lambertson *et al*, 1999; Saeki *et al*, 2002). However, yeast can survive when both *RAD23* and *DSK2* genes are mutated, suggesting that other mechanisms or molecule(s) possessing a shuttle function exist (Saeki *et al*, 2002). Here, we show that ZNF216, a novel ubiquitin-binding protein containing an A20-type zinc-finger, is such a factor. *Znf216* expression is upregulated in skeletal muscle in experimental models of muscle atrophy, and *Znf216*-deficient mice exhibit resistance to muscle atrophy accompanied by abnormal accumulation of polyubiquitinylated proteins in skeletal muscle. Our findings suggest that ZNF216, with its potential function of anchoring ubiquitinylated proteins to the proteasome, plays a critical role in degrading muscle proteins.

*Corresponding author. Department of Bone & Joint Disease, National Center for Geriatrics & Gerontology (NCGG), Obu, Aichi 474-8522, Japan. Tel.: +81 562 46 2311; Fax: +81 562 44 6595;
E-mail: kwatanab@nils.go.jp

Received: 6 June 2005; accepted: 14 December 2005; published online: 19 January 2006

Results

ZNF216 directly binds to polyubiquitin

We have identified a gene, *Znf216* (*Za20d2*, Mouse Genome Informatics), encoding an A20 zinc-finger (Znf-A20) motif-containing protein, as a RANKL-induced gene upregulated upon osteoclast formation using a microarray technique (Hishiya *et al*, 2005). *Znf216* was originally identified as a candidate gene for hearing loss and is expressed in cochlear and skeletal muscle (Scott *et al*, 1998; Huang *et al*, 2004). To determine the function of ZNF216, we searched for molecules that associate with ZNF216 using yeast two-hybrid screening and isolated several clones encoding a gene for polyubiquitin C. To determine whether ZNF216 interacts with ubiquitin in mammalian cells, we transfected HEK293 cells with an expression vector for FLAG-tagged ZNF216 and HA-tagged ubiquitin and performed co-immunoprecipitation experiments. ZNF216 possesses A20-type (amino acids 11–35) and AN1-type (amino acids 154–191) zinc-finger domains at its N- and C-termini, respectively (Figure 1A). Endogenous ubiquitinylated proteins, which appear as smears, were co-immunoprecipitated with FLAG-tagged ZNF216 (Figure 1B). Notably, N-terminal deletion (ΔN; amino acids 36–213) or point mutants (M1 and M3) of the A20-type zinc-finger (ZnF-A20) domain abolished ubiquitin-binding ability of ZNF216, indicating that the ZnF-A20 domain is indispensable for binding to ubiquitin (Figures 1A and B). Whereas in non-denaturing conditions, ubiquitinylated molecules were present with FLAG-tagged ZNF216, these molecules completely disappear from immunoprecipitates following heat denaturation, which abolishes noncovalent protein–protein interactions (Figure 1C), suggesting that ZNF216 associates with ubiquitinylated proteins rather than being ubiquitinylated itself. Next, to determine whether ZNF216 binds to ubiquitin directly, we performed GST pull-down assays using GST-ZNF216 fusion proteins (Figure 1D) and purified polyubiquitin. As shown in Figure 1E, GST-ZNF216 but not GST bound to polyubiquitin chains. As expected, binding of ZNF216 to polyubiquitin chains was completely abolished by a point mutation in the ZnF-A20 domain (M1, Figure 1E). Furthermore, a GST fusion protein containing only the ZnF-A20 domain (amino acids 2–60) could bind to polyubiquitin chains, suggesting that ZNF216 directly binds to polyubiquitin chains, and that the ZnF-A20 domain is required for binding to polyubiquitin. As for other ZnF-A20 containing proteins, AWP1 (ZA20D3) also possessed polyubiquitin-binding activity but the ZnF-A20 domain(s) of Rabex-5 (Horiuchi *et al*, 1997) and A20/TNFAIP3 (Opipari *et al*, 1990) proteins did not (Supplementary Figure S1).

ZNF216 associates with the 26S proteasome

We also identified molecules associating with ZNF216 by proteomic analysis of complexes formed with FLAG-tagged ZNF216. Molecules expressed in HEK293 cells and that co-immunoprecipitated with FLAG-tagged ZNF216 were analyzed by tandem mass spectrometry. By this analysis, every subunit of the 26S proteasome complex was identified as associating with FLAG-tagged ZNF216 (data not shown). To identify the region of ZNF216 required for association with the 26S proteasome, lysates of cells expressing either FLAG-tagged ZNF216 or its mutants were immunoprecipitated with anti-FLAG antibody. Co-precipitation of proteasomal components was monitored by immunoblotting using an antibody against Rpn7p (S10a), a non-ATPase subunit of the 19S regulatory subunit. As shown in Figure 2A, this protein efficiently co-precipitated with FLAG-tagged ZNF216. The interaction was also observed with truncated or point mutants of ZnF-A20 (ΔN or M1), indicating that ubiquitin-binding ability is dispensable for association with the 26S proteasome. To determine whether endogenous ZNF216 proteins are also associated with the 26S proteasome, we performed a GST pull-down assay using the ubiquitin-like (Ubl) domain of hHR23B, a human homologue of Rad23, which is known to bind to the 26S proteasome. As shown in Figure 2B, GST-Ubl but not GST was pulled down with the endogenous 26S proteasome. Endogenous ZNF216 was also detected in the GST-Ubl/26S proteasome complex (upper panels, Figure 2B). Furthermore, purified recombinant ZNF216 did not bind to GST-Ubl (lower panel, Figure 2B), suggesting that endogenous ZNF216 is not directly bound to the Ubl domain but associates with the 26S proteasome.

Colocalization with the aggresome

Next, we determined the subcellular localization of ZNF216. Indirect immunofluorescence of ZNF216 expressed in COS-7 cells showed that the protein was largely cytoplasmic but was seen to a lesser extent in the nucleus (Figure 3A). Aggresomes, which are insoluble aggregates of ubiquitinylated proteins complexed with the proteasome and induced by treatment with proteasome inhibitors, are known to mimic inclusions seen in pathogenic UPS disorders (Johnston *et al*, 1998; Kopito, 2000; Lelouard *et al*, 2002). As shown in Figures 3D–H, ZNF216 proteins were colocalized with aggresomes induced by treatment with the proteasome inhibitor MG132. ZNF216 itself was not ubiquitinylated as shown in Figure 1C.

Induction of ZNF216 expression upon muscle atrophy

Biochemical and cell biological evidence presented here strongly suggests that ZNF216 functions in the UPS. In skeletal muscle, it is generally accepted that the UPS plays a critical role in muscular atrophy, and expression of atrophy-related genes including those encoding UPS components is induced in atrophying muscle (Jagoe *et al*, 2002; Lecker *et al*, 2004). As *Znf216* was predominantly expressed in brain and skeletal muscle (Scott *et al*, 1998), we investigated the relationship between ZNF216 and muscle atrophy. To determine whether *Znf216* expression is induced during muscle atrophy, an *in vitro* model of muscle atrophy was utilized. It has been reported that addition of dexamethasone to cultures of differentiated C2C12 myotubes causes formation of myotubes exhibiting signs of atrophy, including a reduction in myotube diameter (Stitt *et al*, 2004). Such treatment dramatically induced expression of *Znf216* (Figure 4A).

Next, expression of *Znf216* was determined in *in vivo* experimental models of muscle atrophy. Mice that undergo fasting for 2 days show significant decreases in body weight, as well as in the mass of the gastrocnemius muscles (data not shown). In this model, fasting for 2 days results in dramatic increases in *Znf216* mRNA (Figure 4B) and protein (Supplementary Figure S3) in muscle. Although there were differences in induction patterns of two differently sized transcripts of Znf216 by atrophy-inducting stimuli, both transcripts encode the same protein (Supplementary Figures

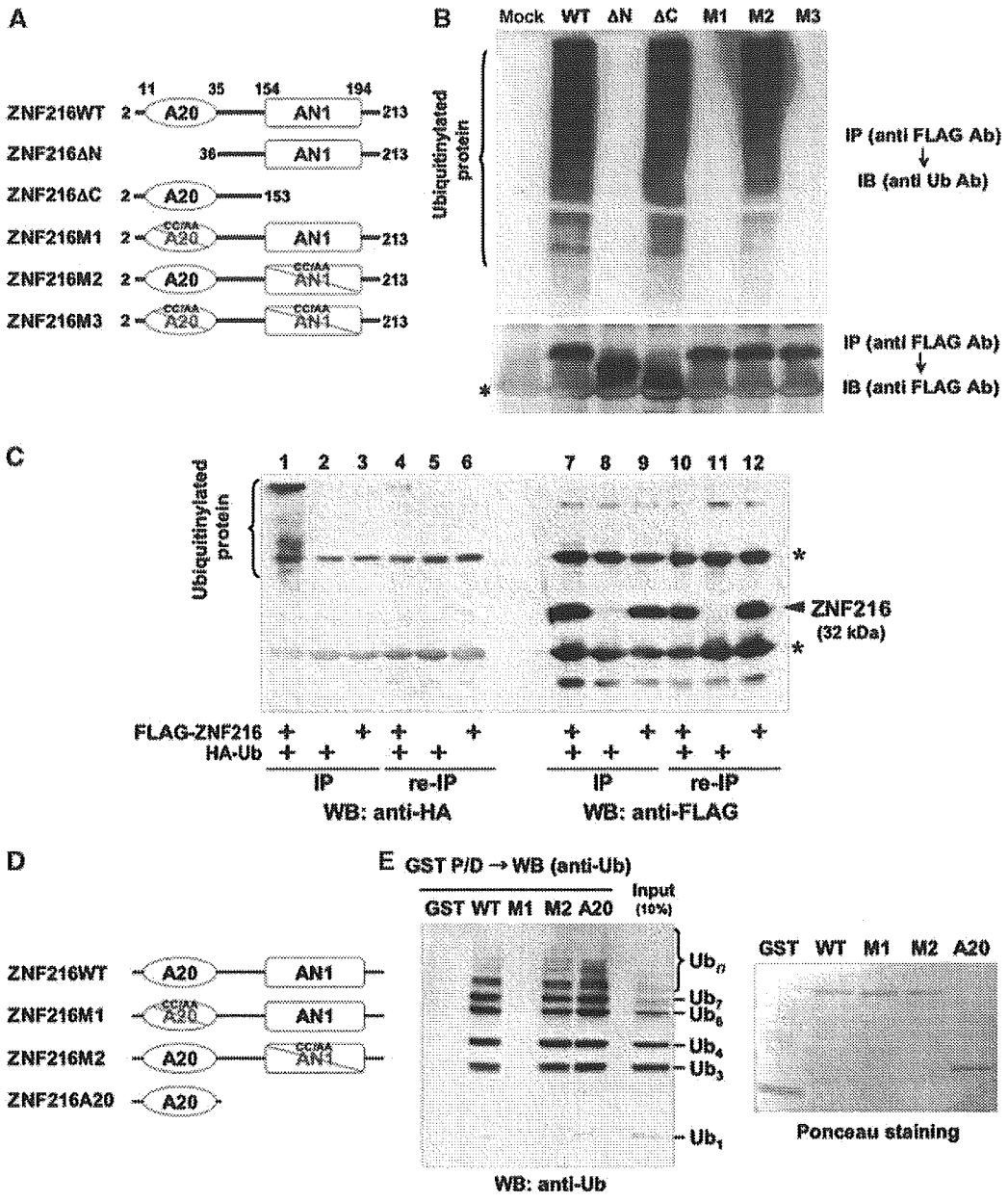

Figure 1 ZNF216 binds polyubiquitin directly through the ZnF-A20 domain. (**A**) Schematic representation of the primary structure of wild-type ZNF216 and its mutants. ZNF216ΔN (aa 36–213) and ZNF216ΔC (aa 2–153) constructs lack the ZnF-A20 (aa 11–35) and ZnF-AN1 (aa 154–194) domains, respectively. Cysteine residues at positions 30 and 33 within the ZnF-A20 were substituted with alanines (C30A/C33A) in ZNF216M1, and both cysteines 170 and 175 within the ZnF-AN1 were substituted with alanines (C170A/C175A) in ZNF216M2. Both ZnF-A20 and ZnF-AN1 domains were mutated in ZNF216M3. (**B**) Co-precipitation of ubiquitinylated proteins and ZNF216. FLAG-tagged ZNF216 or mutants were expressed in HEK293 cells, and cell extracts were immunoprecipitated with anti-FLAG antibody. Ubiquitinylated proteins detected with anti-ubiquitin antibody were precipitated with FLAG-tagged ZNF216 but not with ZnF-A20 mutants. Expression levels of FLAG-tagged ZNF216 constructs are shown at the bottom. Bands corresponding to immunoglobulin chains are marked by an asterisk. (**C**) ZNF216 is minimally ubiquitinylated. HEK293 cells expressing FLAG-tagged ZNF216 or HA-tagged ubiquitin were lysed and immunoprecipitation was performed using anti-FLAG antibody. Aliquots of precipitated beads were boiled and immunoprecipitated again (re-IP). Each sample was separated on gels and probed with anti-HA (left) or anti-FLAG antibody (right). Bands for immunoglobulin chains are marked by asterisks. (**D**) Constructs used for *in vitro* binding assay. ZNF216WT, ZNF216M1 and ZNF216 M2 were as indicated in (A). ZNF216A20 possesses only the A20 domain (aa 2–60). All constructs were produced as GST fusion proteins. (**E**) *In vitro* ubiquitin binding assay. Left panel: GST protein fused to the constructs indicated in (D) was incubated with purified K48-linked polyubiquitin chains, followed by precipitation with GSH beads. In all, 10% of purified polyubiquitin chains was separated without pull-down to evaluate protein amount (10% input). Right panel: the membrane was stained with ponceau to evaluate levels of GST fusion protein.

S2 and S3). Expression of MuRF-1 (Figure 4B) and MAFbx (Gomes *et al*, 2001) was also induced in fasting. Upregulation of *Znf216* was also observed in a model of denervation-induced muscle atrophy. Neurectomy promotes significant reduction (~20%) in the weight of gastrocnemius muscles within the first 7 days postsurgery. As expected, expression of *Znf216* and MuRF-1 was induced in gastrocnemius muscles by denervation-induced muscle atrophy (Figure 4C). These results suggest that *Znf216* expression is associated with atrophy in skeletal muscles.

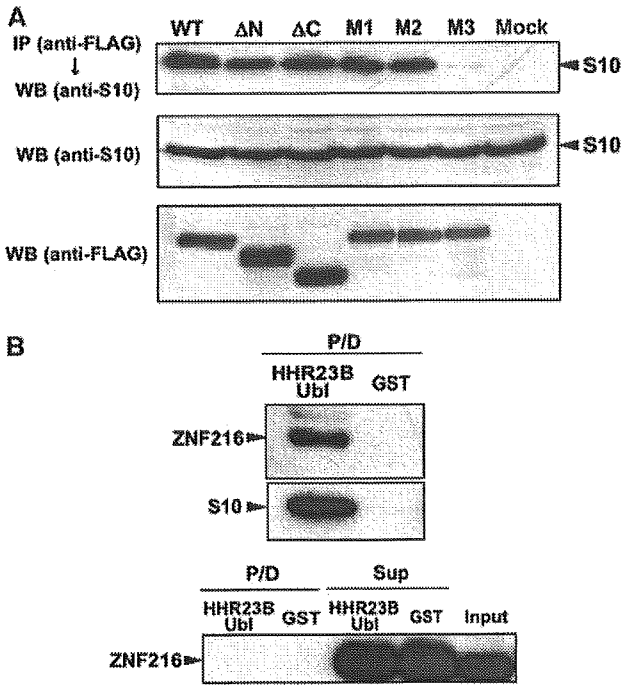

Figure 2 Interaction of ZNF216 with the 26S proteasome in mammalian cells. (**A**) Co-precipitation of the 26S proteasome and ZNF216. Co-precipitated proteins with FLAG-ZNF216 were resolved by SDS–PAGE and detected by immunoblotting using anti-S10a/Rpn7p antibody (anti-S10) or anti-FLAG antibody. Aliquots of cellular extracts were immunoblotted without immunoprecipitation to evaluate protein expression in the bottom panels. (**B**) ZNF216 was detected in the 26S proteasome fraction. Upper panel, cell lysates were incubated with a GST fusion of HHR23B Ubl (HHR23B Ubl) to isolate the 26S proteasome. Precipitated proteins (P/D) were separated and probed with anti-S10 or anti-ZNF216 antibody. Lower panel: purified recombinant ZNF216 was incubated with a GST fusion of HHR23B Ubl or GST protein. Precipitated (P/D) or not precipitated (Sup) proteins were probed with anti-ZNF216 antibody. No direct binding of ZNF216 to the Ubl domain of HHR23B was detected.

The transcription factor FOXO has been reported to play a critical role in muscular atrophy by inducing atrophy-related genes, including MAFbx/Atrogin-1 (Sandri *et al*, 2004; Stitt *et al*, 2004). Therefore, we asked whether FOXO activation upregulated *Znf216* expression. To do so, we employed a Cre-loxP system (Furukawa-Hibi *et al*, 2002) in which constitutively active FOXO4 (AFX-TM) created by mutation of the three Akt phosphorylation sites, T32A, S253A and S315A (Brunet *et al*, 1999), was expressed in C2C12-AFX-TM cells following infection by Cre recombinase-expressing adenovirus (Cre) (Figure 4D). Both AFX-TM mRNA and protein were induced 24 h after infection with Cre but not with control adenovirus (Furukawa-Hibi *et al*, 2002). ZNF216 mRNA was markedly increased in C2C12-AFX-TM cells as a result of infection with Cre but not following infection with control virus (Figure 4E). These results suggest that ZNF216 may function as a downstream effector of FOXO in muscle atrophy.

Generation of mice lacking ZNF216

To investigate the *in vivo* function of ZNF216, mice deficient for ZNF216 ($Znf216^{lex/lex}$) were generated by gene trapping at Omnibank of Lexicon Genetics (Zambrowicz *et al*, 1998). The structure of the predicted trapped gene is shown in Figure 5A. The trapping vector, VICTR48, was inserted 3.3 kbp upstream of exon 3, which encodes the first methionine of mouse *Znf216* (Figure 5A). $Znf216^{lex/lex}$ mice were born from interbred heterozygous $Znf216^{+/lex}$ mice in Mendelian ratios, indicating that ZNF216 is dispensable for embryogenesis or fetal development. No ZNF216 mRNA or protein was detected in $Znf216^{lex/lex}$ mice by Northern or immunoblot analyses, respectively (Figures 5B and C), indicating that the mice are ZNF216 nulls. Expression levels of ZNF216 in $Znf216^{+/lex}$ heterozygotes were nearly one-half those of wild-type mice. $Znf216^{lex/lex}$ mice were viable and fertile, without gross abnormalities or apparent pathological alteration, but they weighed less than sex- and age-matched controls (Figure 5D). At 45 weeks, the average weights of $Znf216^{+/+}$ and

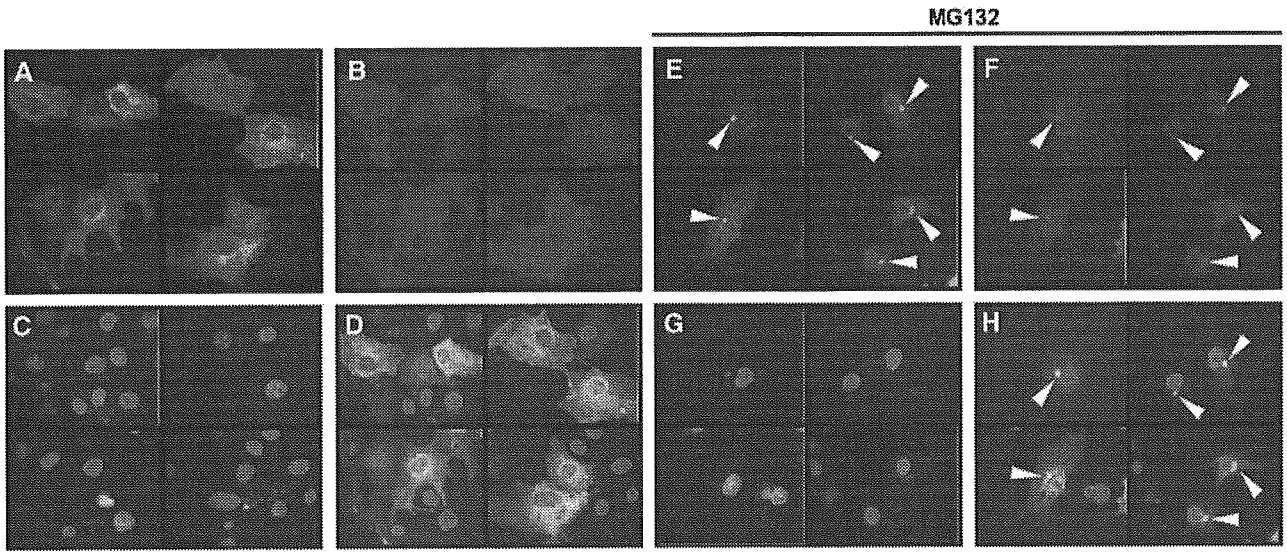

Figure 3 ZNF216 is localized in 'aggresomes' with ubiquitinylated proteins. (**A–H**) COS cells were transfected with expression vectors for FLAG-tagged ZNF216 and HA-tagged ubiquitin. Fixed cells were subjected to indirect immunofluorescence using (A, E) anti-FLAG (with AlexaFluor 488 anti-mouse IgG, green) and (B, F) anti-HA (with AlexaFluor 546 anti-rat IgG antibodies, red) antibodies. (C, G) Nuclei were stained with DAPI in the same fields of each panel. (E–H) Transfected COS cells were treated with the proteasome inhibitor, MG132 (0.5 μM). Aggresomes formed are indicated by arrowheads. The merged images were shown in (D and H).

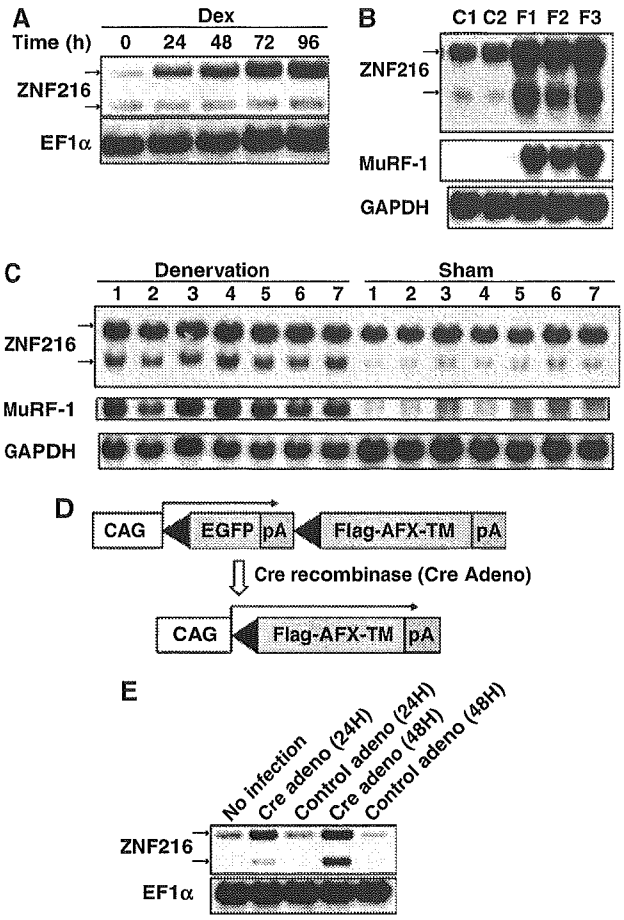

Figure 4 Expression of ZNF216 is induced by muscle atrophy. (**A**) C2C12 myoblast cells were differentiated into myotubes, and treated with 100 μM Dex for the indicated times. Northern blotting was performed to reveal the effect of Dex on ZNF216 expression. The entire coding region of ZNF216 was used as a probe, which recognized 2.4 and 1.5 kb mRNA species arising from alternative splicing and polyadenylation. The loading control was elongation factor α (EF1α). (**B**) Fasting-induced muscle atrophy. Three mice were fasted (F1 ~ F3), and two mice (C1, C2) were fed freely. After 2 days, RNA was purified from gastrocnemius muscle, and Northern blotting was performed to determine ZNF216 expression. The membrane was re-probed with MuRF-1 and GAPDH. (**C**) Denervation-induced muscle atrophy was induced by cutting the sciatic nerve of the hindlimb of seven mice (1 ~ 7). The opposite limb was sham operated as the control. At 7 days after surgery, total RNA was purified from gastrocnemius muscles, and Northern blotting was performed to detect ZNF216 expression. The membrane was re-probed with MuRF-1 and GAPDH. (**D**) Cre-loxP-mediated, constitutively active FOXO expression system. cDNA encoding FLAG-tagged constitutively active FOXO4 (AFX-TM) is separated from the CAG promoter of an expression vector by a loxP-flanked EGFP-poly(A) cassette. Infection with adenovirus expressing Cre recombinase (Cre) results in excision of the DNA fragment located between the two loxP sequences and expression of FLAG-tagged AFX-TM. (**E**) ZNF216 is downstream of FOXO. Total RNAs were prepared from C2C12-AFX-TM cells at the indicated times after infection with adenovirus expressing Cre (Cre) or lacZ (control) and probed by *Znf216* or EF1α. A marked increase in expression of *Znf216* was observed only in Cre-infected cells.

Znf216$^{lex/lex}$ male mice were 42.66 ± 7.06 g ($n = 14$) and 33.16 ± 4.44 g ($n = 9$), respectively. The average weights of female *Znf216*$^{+/+}$ and *Znf216*$^{lex/lex}$ mice were 34.46 ± 4.21 g ($n = 14$) and 26.85 ± 5.38 g ($n = 11$), respectively. After 30 weeks, both female and male *Znf216*$^{lex/lex}$ mice showed no or subtle increases in weight, whereas *Znf216*$^{+/+}$ or

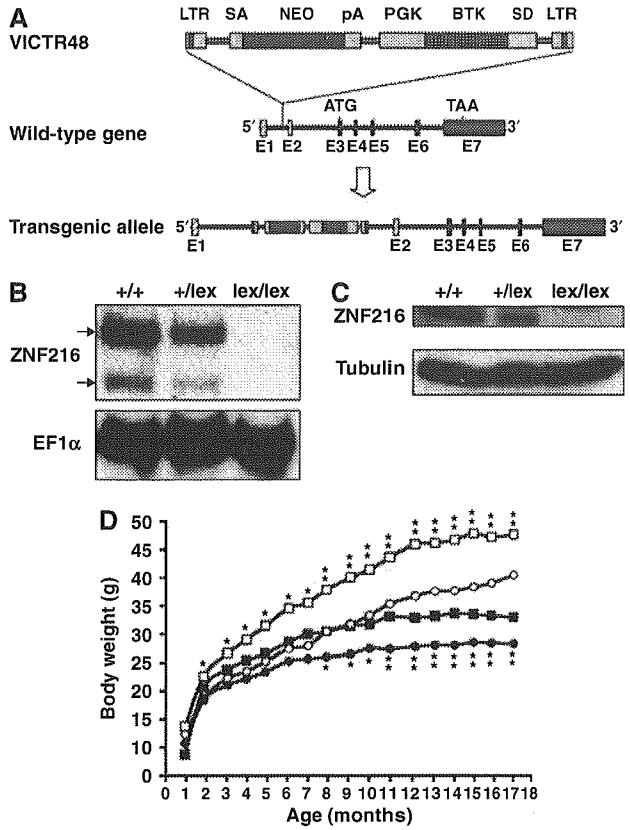

Figure 5 Disruption of *Znf216* gene in mice. (**A**) Gene trap strategy of *Znf216* gene. The structure of the trapping vector, VICTR48, is shown in the upper line. The wild-type allele and the trapped, transgenic allele follow the vector. The retroviral vector, VICTR48, was integrated between exons 1 and 2 of the *Znf216* gene and transcription of downstream exons encoding ZNF216 was diminished. Exons are depicted by striped (noncoding exons) or shadowed boxes (protein-coding exons) and numbered (E1 and E2). LTR, long terminal repeat; SA, splice acceptor site; SD, splice donor site; pA, polyadenylation signal; PGK, PGK promoter. (**B**) Northern blot analysis. Total RNA was prepared from brains of *Znf216*$^{+/+}$, *ZnfF216*$^{+/lex}$ or *Znf216*$^{lex/lex}$ mice. Full-length mouse ZNF216 cDNA was used as a probe. The membrane was re-probed using an EF1α probe. (**C**) Immunoblot analysis. Extracts from brain of *Znf216*$^{+/+}$, *Znf216*$^{+/lex}$ or *Znf216*$^{lex/lex}$ mice were immunoblotted with antibody against ZNF216. The membrane was re-probed using anti-tubulin antibody. (**D**) Growth curve of *Znf216*$^{lex/lex}$ mice. Body weights at each time point of *Znf216*$^{+/+}$ and *Znf216*$^{lex/lex}$ mice were indicated as open square boxes (males) or circles (females) and closed square boxes (males) or circles (females), respectively. $^{*}P < 0.05$; $^{**}P < 0.005$.

Znf216$^{+/lex}$ mice gained weight as they aged (Figure 5D). The size of most organs in *Znf216*$^{lex/lex}$ mice was reduced in proportion with body weight. However, the fat volume of aged (> 30 weeks of age) *Znf216*$^{lex/lex}$ mice was significantly decreased, suggesting that the marked difference in body weight between wild-type and aged *Znf216*$^{lex/lex}$ mice is mainly caused by decreased fat mass seen in *Znf216*$^{lex/lex}$ mice (not shown). Detailed phenotypic characterization of aged mutant mice will be provided elsewhere.

Znf216$^{lex/lex}$ mice exhibit partial resistance to denervation-induced muscle atrophy

To further explore the involvement of ZNF216 in muscle atrophy, neurectomy of sciatic nerve was undertaken in wild-type and *Znf216*$^{lex/lex}$ mice. As shown in Figure 6A, 7

days after denervation, significant muscle weight loss and reduction in fiber sizes of the gastrocnemius muscle were observed in wild-type mice. By contrast, such decreases in muscle weight were significantly attenuated in *Znf216*$^{lex/lex}$ mice (Figure 6A). Sections of gastrocnemius muscle also showed larger fibers in muscle from neurectomized *Znf216*$^{lex/lex}$ mice than in control muscle (Figure 6B). However, there was no significant difference in fiber area between sham-operated wild-type and *Znf216*$^{lex/lex}$ mice (wild type + sham operated, $1988 \pm 530\,\mu m^2$; wild type + denervation, $1379 \pm 345\,\mu m^2$; lex/lex + sham operated, $1776 \pm 484\,\mu m^2$; lex/lex + denervation, $1393 \pm 344\,\mu m^2$). As shown in Figure 6C, the reduction in fiber area was also less apparent in *Znf216*$^{lex/lex}$ mice compared to wild-type mice. These results suggest that ZNF216 plays a crucial role in reduction of muscle mass on denervation-induced muscle atrophy.

Abnormal accumulation of ubiquitinylated proteins in muscle from Znf216$^{lex/lex}$ *mice*

To investigate what abnormalities occur during denervation-induced muscle atrophy in *Znf216*$^{lex/lex}$ mice, we examined

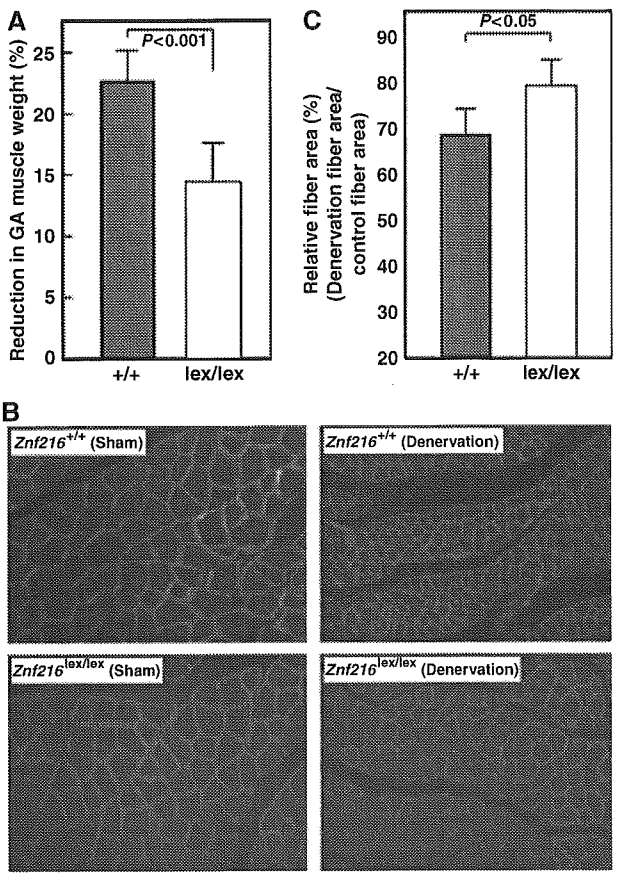

Figure 6 Denervation induced muscular atrophy was attenuated in *ZNF216*$^{lex/lex}$ mice. (**A**) Reduction of GA muscle weight upon neurectomy. Percent decreases in muscle weights are shown as a percent of control, calculated as the left/right muscle weights. (**B**) Cross-sections from gastrocnemius muscle were stained by indirect immunofluorescence with anti-laminin. The reduction in size was also significant in muscle fibers of control mice but less in *Znf216*$^{lex/lex}$. (**C**) Muscle fiber cross-sectional areas were measured in transverse tissue section (B). Percent relative fiber area of denervated muscle to control fiber area (sham-operated) are shown.

expression levels of factors involved in muscle atrophy. As expected, expression of MAFbx/Atrogin-1 and MuRF-1 was dramatically induced by denervation-induced muscle atrophy in gastrocnemius muscle from wild-type mice (Figure 6A). In *Znf216*$^{lex/lex}$ mice, expression of MAFbx/Atrogin-1 and MuRF-1 was also induced at levels comparable to those seen in wild-type mice. Induction of *Pmsa1* and *Pmsd11*, genes encoding the 26S proteasome subunits α6 and Rpn6, respectively, was also indistinguishable between *Znf216*$^{lex/lex}$ and wild-type mice (Figure 7A). Furthermore, proteasome activities in gastrocnemius muscles were comparable between wild-type and *Znf216*$^{lex/lex}$ mice (Figure 7B). Thus, induction of relevant ubiquitin ligases or proteasome components was not affected in *Znf216*$^{lex/lex}$ mice. It is known that ubiquitinylated proteins accumulate during muscle atrophy (Medina *et al*, 1991; Wing *et al*, 1995). As shown in Figure 7C, following denervation, ubiquitinylated proteins accumulated in the gastrocnemius muscle of wild-type mice, but higher levels of ubiquitinylated proteins accumulated in muscle derived from *Znf216*$^{lex/lex}$ mice (~2-fold: $P<0.001$ in neurectomized *Znf216*$^{lex/lex}$ versus wild-type muscle). Similar results were obtained by fasting-induced muscle atrophy, although no difference in the levels of ubiquitinylated proteins from controls (sham-operated or fed) was observed between genotypes (Figure 7C). These results indicate that ZNF216 is a critical regulator of muscle atrophy, most likely functioning to regulate degradation of muscle proteins without altering expression of proteasomal components or known E3 ligases.

Effect of ZNF216 on UPS-mediated protein degradation

Accumulation of ubiquitinylated protein under any circumstance might be because of loss of inhibition of ubiquitinylation and/or deubiquitinylation (DUB). However, no inhibition or DUB activity was observed (Supplementary Figures S4 and S5). As shown in Figure 7D, association of ZNF216 protein to the proteasome was significantly increased when atrophy was induced, suggesting that ZNF216 may be involved in association of ubiquitinylated proteins and the proteasome. The biochemical activity of ZNF216 is similar to that of the UPS proteins, hHR23 and hPLIC, both of which have a shuttle function and are known to bind to both polyubiquitinylated proteins and the 26S proteasome (Hartmann-Petersen and Gordon, 2004; Elsasser and Finley, 2005). Interestingly, overexpression of hHR23 and hPLIC results in stabilization of unstable proteins such as p53 (Kleijnen *et al*, 2000; Glockzin *et al*, 2003). To determine if ZNF216 functioned similarly, we employed a degradation system using unstable GFP (Bence *et al*, 2001). In this system, the CL1 peptide, which functions as a degron, is fused to EGFP (EGFP-CL1). Degradation by conjugation with the degron is mediated by the UPS (Bence *et al*, 2001). EGFP-CL1, constitutively expressed in HEK293 cells, is unstable and the estimated half-life ($t_{1/2}$) of EGFP-CL1 in this system is about 11 min. Ubiquitinylated EGFP-CL1 protein stabilized by treatment with a proteasome inhibitor was associated with ZNF216 but EGFP itself was not (not shown). As shown in Figure 8A, protein degradation was markedly retarded in the presence of ectopic ZNF216 ($t_{1/2}>30$ min) compared to cells transfected with the loss of function mutant ZNF216M3 or mock-transfected cells. Rapid turnover of EGFP-CL1 protein was inhibited by treatment with the

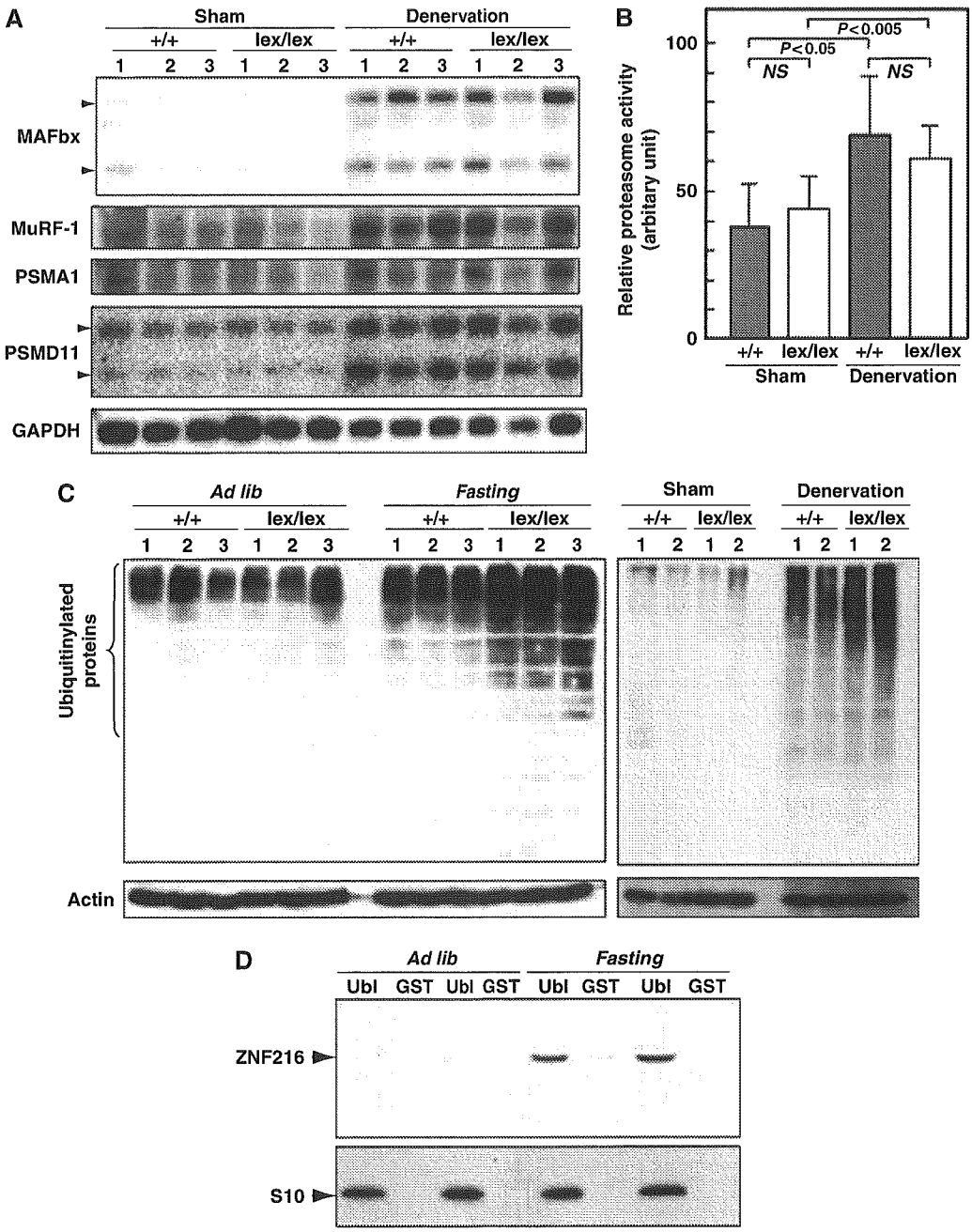

Figure 7 Changes in UPS upon muscular atrophy. (**A**) Expression of UPS components in denervation-induced muscular atrophy. Total RNAs were purified from gastrocnemius muscle, and Northern blotting was performed using indicated probes. Expression of genes for ubiquitin-ligases, such as MAFbx or MuRF-1, and proteasome subunits PSMA1 and PSMD11 was induced by muscle atrophy at comparable levels between wild-type and *ZNF216*$^{lex/lex}$ mice. (**B**) Proteasome activity. Proteasome activities in muscle extracts from wild-type or *ZNF216*$^{lex/lex}$ mice were measured and are shown as arbitrary units. No significant difference in proteasome activity between wild-type and *ZNF216*$^{lex/lex}$ was observed. (**C**) High levels of ubiquitinylated proteins accumulated in muscles from *ZNF216*$^{lex/lex}$ mice than in muscles from wild-type mice. Muscle extracts from wild-type or *ZNF216*$^{lex/lex}$ mice were subjected to immunoblotting using anti-ubiquitin antibody to analyze levels of ubiquitinylated proteins. Left and right panels show fasting-induced and denervation-induced muscle atrophy, respectively. Each membrane was re-probed with anti-actin antibody. (**D**) Association of ZNF216 with the proteasome was increased upon atrophy. The proteasome fractions in muscle extracts from fed (*ad lib*) or fasted (fasting) mice were precipitated with GST-Ubl or GST only as a negative control. Endogenous ZNF216 protein was co-precipitated with the proteasome, which is probed by the anti-S10 antibody.

proteasome inhibitor MG132 (MG132, Figure 8B). The levels of the proteins stabilized by MG132 were comparable among cells transfected with ZNF216 constructs, indicating that protein synthesis of EGFP-CL1 was not significantly affected by ectopic expression of ZNF216 (MG132, Figure 8B). ZNF216WT, and to a lesser extent the mutants M1 and M2 but not M3, attenuated degradation (NT, Figure 8B). Thus, as is the case with other shuttle proteins, overexpression of ZNF216 inhibits degradation of unstable proteins via the UPS.

Discussion

ZNF216 is an atrogene

In this report, we show that *Znf216*$^{lex/lex}$ mice exhibit resistance to denervation-induced muscle atrophy. It has been

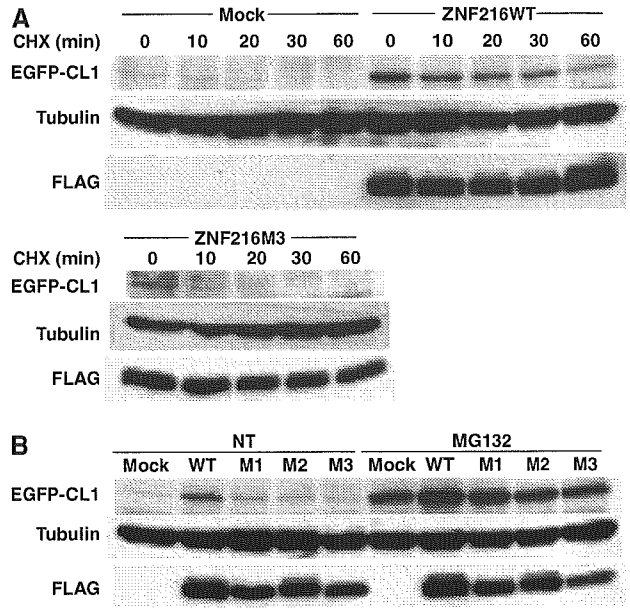

Figure 8 Ectopic expression of ZNF216-affected protein degradation. (**A**) Degradation of EGFP-CL1 protein was delayed by overexpression of ZNF216. 293 cells stably expressing EGFP-CL1 were transfected with plasmid of ZNF216WT, ZNF216M3 or pcDNA3 (mock). Estimated half-lives of the EGFP-CL1 are 35, 11 and 11 min in ZNF216WT-, ZNF216M3- and mock-transfected cells, respectively. *De novo* protein synthesis was arrested by cycloheximide (CHX). The membrane was re-probed with tubulin antibody to control for protein loading (tubulin) and FLAG antibody to detect ZNF216 expression (FLAG). (**B**) Degradation of EGFP-CL1 protein in the presence of various ZNF216 constructs. HEK293 cells stably expressing EGFP-CL1 were transfected with plasmids expressing the indicated mutants. Transfected cells were not treated (NT) or MG132-treated (MG132), and EGFP-CL1 protein was detected with an anti-GFP antibody (EGFP-CL1). The membrane was re-probed with tubulin antibody to control for protein loading (tubulin) and FLAG antibody to detect ZNF216 expression (FLAG).

shown that TNFα induces catabolic conditions through UPS during cancer cachexia (Mitch and Price, 2001). Recently, it has been reported that mice deficient in molecules involved in the NF-κB pathway exhibit resistance to muscular atrophy (Cai *et al*, 2004; Hunter and Kandarian, 2004; McKinnell and Rudnicki, 2004). On the other hand, the IGF-FOXO axis has been suggested to regulate muscle mass through induction of 'atrogenes' such as Murf1 and MAFbx/Atrogin-1 (Sandri *et al*, 2004; Stitt *et al*, 2004). Although we provide evidence that *Znf216* is downstream of FOXO, the NF-κB pathway could represent an alternative signal inducing ZNF216. Indeed, we have identified *Znf216* as a gene induced by RANKL, a TNF family ligand (Hishiya *et al*, 2005) which activates the NF-κB pathway through RANK (Anderson *et al*, 1997; Lacey *et al*, 1998). Moreover, TNFα and IL-1β upregulate expression of ZNF216 in fibroblasts and macrophages (Hishiya *et al*, 2005). These results suggest that *Znf216* may be activated by NF-κB. Huang *et al* (2004) recently reported that ZNF216 inhibits the NF-κB pathway. Whereas treatment with TNFα or overexpression of TRAF6 dramatically activated a reporter driven by NF-κB response elements, ectopic expression of A20/TNFAIP3 but not ZNF216 inhibited NF-κB activation (not shown). Using mouse embryonic fibroblasts, splenocytes or bone marrow cells from $Znf216^{lex/lex}$ or wild-type mice, no significant differences were observed in TNFα-dependent NF-κB activation, LPS-induced cytokine expression or proliferation (unpublished data). Therefore, ZNF216 seems to function as a downstream effector (i.e., a component of the UPS) rather than a specific negative regulator of NF-κB signaling, although ZNF216 function in that pathway is still under investigation. Whereas expression of ZNF216 is not restricted to muscle, such expression was induced upon muscular atrophy and loss of function of *Znf216* promotes resistance to denervation-induced atrophy, thereby suggesting that it fulfills the definition of an 'atrogene'.

As it is in skeletal muscle, ZNF216 is highly expressed in the brain (Scott *et al*, 1998). Aberrations in the UPS have been documented in the pathogenesis of neurodegenerative diseases such as Parkinson's and Huntington's diseases (Ross and Poirier, 2004). Massive accumulation of ubiquitinylated proteins, which are often aggregated and impair the UPS leading to neuronal degeneration, has been observed in these pathogenic conditions (Ciechanover and Brundin, 2003; Korhonen and Lindholm, 2004). In cultured cells, blocking the UPS by proteasome inhibitors leads to accumulation of ubiquitinylated proteins. These ubiquitinylated proteins are then transferred to perinuclear locations and form aggresomes (Johnston *et al*, 1998). As shown here, ZNF216 is localized in aggresomes together with ubiquitinylated proteins. Interestingly, proteomic analysis of a protein complex containing HDAC6, a protein often associated with aggresomes (Kawaguchi *et al*, 2003), showed that the complex included AWP1, a structural homologue of ZNF216 (Seigneurin-Berny *et al*, 2001). Although it is unclear whether ZNF216 is involved in aggresome formation, there is great interest in the role of ZNF216 in the pathogenesis of neurodegenerative diseases.

Molecular function of an A20-containing protein, ZNF216

In muscle atrophy, more ubiquitinylated proteins accumulate in muscle from $Znf216^{lex/lex}$ mice than in muscle from wild-type mice, suggesting an abnormal UPS function. Inhibition of neither polyubiquitinylation nor DUB activity was observed in ZNF216. Although our *in vivo* data showed significant accumulation of polyubiquitinylated proteins in muscle from $Znf216^{lex/lex}$ mice, there is a possibility that ZNF216 is a ubiquitin-ligase. It has been recently reported that A20/TNFAIP3 protein possesses ubiquitin ligase activity against RIP through its ZnF-A20 repeats (Wertz *et al*, 2004). We asked whether the ZnF-A20 of ZNF216 exhibited activity similar to A20/TNFAIP3, but *in vitro* ubiquitinylation assays were negative (Supplementary Figure S6). In fact, the ZnF-A20 of A20/TNFAIP3 protein does not bind polyubiquitin chains as does the ZnF-A20 of ZNF216 (Supplementary Figure S1). Furthermore, there are seven ZnF-A20 motifs in A20/TNFAIP3 and only the fourth is responsible for E3 activity, suggesting that the ZnF-A20 motif is not inherently active enzymatically (Wertz *et al*, 2004). However, we cannot exclude the possibility that ZNF216 may possess DUB or E3 activity highly specific to an unknown substrate without nonspecific or self-ubiquitinylating activity.

ZNF216 likely acts as a bridging or a shuttle factor of ubiquitinylated proteins targeted to the proteasome. Shuttle proteins, such as Rad23p and Dsk2p, share interfaces for ubiquitinylated proteins and the proteasome (Hartmann-Petersen and Gordon, 2004; Elsasser and Finley, 2005).

Although shuttle proteins are required for efficient protein degradation, ectopic expression of hHR23 or hPLIC, the human homologues of Rad23p or Dsk2p, respectively, lead to stabilization of p53 protein (Kleijnen *et al*, 2000; Glockzin *et al*, 2003). These outcomes may be caused by titration effects due to overexpression and are commonly observed following misexpression of shuttle proteins in yeast and mammals (Hartmann-Petersen and Gordon, 2004; Verma *et al*, 2004). Here, we show that ZNF216 has a ubiquitin binding domain and can associate with the 26S proteasome even in the absence of ubiquitin binding, and that overexpression of the zinc-finger protein attenuates protein degradation rate. There is no structural counterpart of ZNF216 in the yeast genome. We asked whether ZNF216 could rescue the bridging function of RAD23 or DSK2 mutants by introducing ZNF216 into Δ*rad23*Δ*dsk2* yeast cells, but the phenotype could not be rescued (data not shown). This suggests that ZNF216 is not the functional orthologue of these proteins. Recently, the presence of an alternative pathway of Rad23p/Dsk2p in protein targeting to the proteasome has been suggested (Bazirgan and Hampton, 2005; Richly *et al*, 2005). It has been reported that tetra-ubiquitin constitutes the minimum proteasomal targeting signal and that the length of polyubiquitin chain may determine the targeting route (Thrower *et al*, 2000; Bazirgan and Hampton, 2005; Richly *et al*, 2005). Notably, ZNF216 preferentially binds polyubiquitin chains longer than di- or tri-ubiquitin (Figure 1D). Therefore, these data suggest that ZNF216 is a novel ubiquitin recognition factor, required for efficient protein degradation via a pathway different from the canonical Rad23p/Dsk2p pathway. Although it is now under investigation, the characterization of ZnF-AN1, an AN1-type zinc-finger domain located at the C-terminus of ZNF216, may reveal the precise molecular function of ZNF216.

Materials and methods

Antibodies

An anti-ZNF216 antibody was raised by immunizing rabbits against synthesized peptide corresponding to the C-terminal sequence of mouse ZNF216. Mouse monoclonal antibodies for FLAG (Sigma, St Louis, MO) and ubiquitin (Santa Cruz Biotechnology, CA), rabbit polyclonal antibodies for ubiquitin (Affiniti Research Products) and actin (Neo Markers, CA), a rat monoclonal antibody for HA (Roche Diagnostics, Mannheim, Germany), and a rabbit polyclonal antibody against S10a/Rpn7p (Affiniti Research Products) were purchased from the indicated manufacturers. For indirect immunofluorescence staining, AlexaFluor 488 goat anti-mouse IgG or AlexaFluor 546 goat anti-rat IgG antibody was obtained from Molecular Probes, OR.

Identification of interacting proteins

RNA was purified from RAW264.7 cells stimulated by RANKL, and used to construct the yeast library (MatchMaker Library Construction & Screening Kit, Clontech). Yeast two-hybrid screening with pGBKT7-ZNF216 was performed as described previously (Masuda *et al*, 2001). Identification of the co-immunoprecipitated proteins with N- or C-terminally FLAG-tagged ZNF216 (ZA20D2) or AWP1 (ZA20D3) was essentially done by a nano-LC/MS/MS system as previously described (Natsume *et al*, 2002; Komatsu *et al*, 2004).

Experimental models of muscle atrophy

For fasting-induced muscle atrophy, 8-week-old C57BL6 male mice were deprived of food but given free access to water. After 2 days, gastrocnemius muscles were harvested for each experiment. Denervation-induced muscle atrophy was performed by dissecting the sciatic nerve of one hindlimb, and the other hindlimb was sham operated as the control. After 7 days, the contralateral normal and denervated gastrocnemius muscles were harvested for each experiment. All animal experiments were approved in advance by the Ethics Review Committee for Animal Experimentation of the National Institute for Longevity Sciences and the National Center for Geriatrics and Gerontology. Student's *t*-tests were used to evaluate statistical differences between the two groups.

Znf216-deficient mice

Generation of heterozygous $Znf216^{+/lex}$ mice was essentially done by the gene trap method at Lexicon Genetics (Zambrowicz *et al*, 1998). Briefly, ES cells heterozygous for the trapped *Znf216* gene were microinjected into eight-cell-stage ICR mouse embryos and transplanted into uteri. Chimeric mice were crossed to C57BL/6J mice. Northern and immunoblot analyses confirmed disruption of the gene (see text). For genotyping, primers were as follows: KO-A, ACCGACAGGATAGACAATGGCAGAG; KO-B, CGATTTTAAGAAAG GAGGCTCTGACC; LTR2, AAATGGCGTTACTTAAGCTAGCTTGC. The wild-type and inserted alleles were detected by PCR using KO-A and KO-B (0.5 kb), and LTR2 and KO-B (0.3 kb), respectively.

EGFP-CL1 degradation assay

The nucleotide sequence encoding the CL1 peptide (ACKNWFSSLSHFVIHL) (Gilon *et al*, 1998) was inserted into the *Xho*I/*Eco*RI site of pEGFP-C3, and the resulting plasmid was designated pEGFP-CL1. A cell line stably expressing EGFP-CL1 (293EGFP-CL1) was generated by transfection of pEGFP-CL1 into 293 cells. For the degradation assay, ZNF216 expression vectors were transfected into 293EGFP-CL1 cells and cells were harvested 48 h after transfection. MG132 (final 10 μM) or cycloheximide (final 100 μg/ml) was added to the culture at 12 or 1 h before harvest, respectively. Protein extraction was as described above.

For more details on supplementary Materials and methods, see Supplementary data

Supplementary data

Supplementary data are available at *The EMBO Journal* Online.

Acknowledgements

We are grateful to Drs Kazuhiro Iwai (Osaka City University) and Noboru Motoyama (NCGG) for reagents, helpful comments and suggestions throughout this study. We also thank Drs Akio Matsuda and Tatsuo Furuyama for experimental instruction and advice; Dr Aya Sasaki for pathological determinations; Ms Miho Kamiya and Ms Kumi Tsutsumi for technical assistance; and Dr Elise Lamar for proofreading the manuscript. This study is supported in part by the Program for Promotion of Fundamental Studies in Health Sciences of the Organization for Pharmaceutical Safety and Research of Japan, and by a Research Grant for Longevity Sciences from the Ministry of Health, Labor and Welfare.

References

Anderson DM, Maraskovsky E, Billingsley WL, Dougall WC, Tometsko ME, Roux ER, Teepe MC, DuBose RF, Cosman D, Galibert L (1997) A homologue of the TNF receptor and its ligand enhance T-cell growth and dendritic-cell function. *Nature* **390:** 175–179

Bailey JL, Wang X, England BK, Price SR, Ding X, Mitch WE (1996) The acidosis of chronic renal failure activates muscle proteolysis in rats by augmenting transcription of genes encoding proteins of the ATP-dependent ubiquitin-proteasome pathway. *J Clin Invest* **97:** 1447–1453

Bazirgan OA, Hampton RY (2005) Cdc48-Ufd2-Rad23: the road less ubiquitinated? *Nat Cell Biol* **7:** 207–209

Bence NF, Sampat RM, Kopito RR (2001) Impairment of the ubiquitin-proteasome system by protein aggregation. *Science* **292:** 1552–1555

Bodine SC, Latres E, Baumhueter S, Lai VK, Nunez L, Clarke BA, Poueymirou WT, Panaro FJ, Na E, Dharmarajan K, Pan ZQ, Valenzuela DM, DeChiara TM, Stitt TN, Yancopoulos GD, Glass DJ (2001) Identification of ubiquitin ligases required for skeletal muscle atrophy. *Science* **294:** 1704–1708

Brunet A, Bonni A, Zigmond MJ, Lin MZ, Juo P, Hu LS, Anderson MJ, Arden KC, Blenis J, Greenberg ME (1999) Akt promotes cell survival by phosphorylating and inhibiting a Forkhead transcription factor. *Cell* **96:** 857–868

Cai D, Frantz JD, Tawa Jr NE, Melendez PA, Oh BC, Lidov HG, Hasselgren PO, Frontera WR, Lee J, Glass DJ, Shoelson SE (2004) IKKbeta/NF-kappaB activation causes severe muscle wasting in mice. *Cell* **119:** 285–298

Chen L, Shinde U, Ortolan TG, Madura K (2001) Ubiquitin-associated (UBA) domains in Rad23 bind ubiquitin and promote inhibition of multi-ubiquitin chain assembly. *EMBO Rep* **2:** 933–938

Ciechanover A, Brundin P (2003) The ubiquitin proteasome system in neurodegenerative diseases: sometimes the chicken, sometimes the egg. *Neuron* **40:** 427–446

Elsasser S, Finley D (2005) Delivery of ubiquitinated substrates to protein-unfolding machines. *Nat Cell Biol* **7:** 742–749

Funakoshi M, Sasaki T, Nishimoto T, Kobayashi H (2002) Budding yeast Dsk2p is a polyubiquitin-binding protein that can interact with the proteasome. *Proc Natl Acad Sci USA* **99:** 745–750

Furukawa-Hibi Y, Yoshida-Araki K, Ohta T, Ikeda K, Motoyama N (2002) FOXO forkhead transcription factors induce G(2)-M checkpoint in response to oxidative stress. *J Biol Chem* **277:** 26729–26732

Gilon T, Chomsky O, Kulka RG (1998) Degradation signals for ubiquitin system proteolysis in Saccharomyces cerevisiae. *EMBO J* **17:** 2759–2766

Glickman MH, Ciechanover A (2002) The ubiquitin-proteasome proteolytic pathway: destruction for the sake of construction. *Physiol Rev* **82:** 373–428

Glockzin S, Ogi FX, Hengstermann A, Scheffner M, Blattner C (2003) Involvement of the DNA repair protein hHR23 in p53 degradation. *Mol Cell Biol* **23:** 8960–8969

Gomes MD, Lecker SH, Jagoe RT, Navon A, Goldberg AL (2001) Atrogin-1, a muscle-specific F-box protein highly expressed during muscle atrophy. *Proc Natl Acad Sci USA* **98:** 14440–14445

Hartmann-Petersen R, Gordon C (2004) Protein degradation: recognition of ubiquitinylated substrates. *Curr Biol* **14:** R754–R756

Hershko A, Ciechanover A (1998) The ubiquitin system. *Annu Rev Biochem* **67:** 425–479

Hishiya A, Ikeda K, Watanabe K (2005) A RANKL-inducible gene Znf216 in osteoclast differentiation. *J. Receptor Signal Transduct* **25:** 199–216

Horiuchi H, Lippe R, McBride HM, Rubino M, Woodman P, Stenmark H, Rybin V, Wilm M, Ashman K, Mann M, Zerial M (1997) A novel Rab5 GDP/GTP exchange factor complexed to Rabaptin-5 links nucleotide exchange to effector recruitment and function. *Cell* **90:** 1149–1159

Huang J, Teng L, Li L, Liu T, Li L, Chen D, Xu LG, Zhai Z, Shu HB (2004) ZNF216 is an A20-like and IkappaB kinase gamma-interacting inhibitor of NFkappaB activation. *J Biol Chem* **279:** 16847–16853

Hunter RB, Kandarian SC (2004) Disruption of either the Nfkb1 or the Bcl3 gene inhibits skeletal muscle atrophy. *J Clin Invest* **114:** 1504–1511

Jagoe RT, Lecker SH, Gomes M, Goldberg AL (2002) Patterns of gene expression in atrophying skeletal muscles: response to food deprivation. *FASEB J* **16:** 1697–1712

Johnston JA, Ward CL, Kopito RR (1998) Aggresomes: a cellular response to misfolded proteins. *J Cell Biol* **143:** 1883–1898

Kawaguchi Y, Kovacs JJ, McLaurin A, Vance JM, Ito A, Yao TP (2003) The deacetylase HDAC6 regulates aggresome formation and cell viability in response to misfolded protein stress. *Cell* **115:** 727–738

Kleijnen MF, Shih AH, Zhou P, Kumar S, Soccio RE, Kedersha NL, Gill G, Howley PM (2000) The hPLIC proteins may provide a link between the ubiquitination machinery and the proteasome. *Mol Cell* **6:** 409–419

Komatsu M, Chiba T, Tatsumi K, Iemura S, Tanida I, Okazaki N, Ueno T, Kominami E, Natsume T, Tanaka K (2004) A novel protein-conjugating system for Ufm1, a ubiquitin-fold modifier. *EMBO J* **23:** 1977–1986

Kopito RR (2000) Aggresomes, inclusion bodies and protein aggregation. *Trends Cell Biol* **10:** 524–530

Korhonen L, Lindholm D (2004) The ubiquitin proteasome system in synaptic and axonal degeneration: a new twist to an old cycle. *J Cell Biol* **165:** 27–30

Lacey DL, Timms E, Tan HL, Kelley MJ, Dunstan CR, Burgess T, Elliott R, Colombero A, Elliott G, Scully S, Hsu H, Sullivan J, Hawkins N, Davy E, Capparelli C, Eli A, Qian YX, Kaufman S, Sarosi I, Shalhoub V, Senaldi G, Guo J, Delaney J, Boyle WJ (1998) Osteoprotegerin ligand is a cytokine that regulates osteoclast differentiation and activation. *Cell* **93:** 165–176

Lambertson D, Chen L, Madura K (1999) Pleiotropic defects caused by loss of the proteasome-interacting factors Rad23 and Rpn10 of *Saccharomyces cerevisiae*. *Genetics* **153:** 69–79

Lecker SH, Jagoe RT, Gilbert A, Gomes M, Baracos V, Bailey J, Price SR, Mitch WE, Goldberg AL (2004) Multiple types of skeletal muscle atrophy involve a common program of changes in gene expression. *FASEB J* **18:** 39–51

Lecker SH, Solomon V, Mitch WE, Goldberg AL (1999) Muscle protein breakdown and the critical role of the ubiquitin–proteasome pathway in normal and disease states. *J Nutr* **129:** 227S–237S

Lelouard H, Gatti E, Cappello F, Gresser O, Camosseto V, Pierre P (2002) Transient aggregation of ubiquitinated proteins during dendritic cell maturation. *Nature* **417:** 177–182

Masuda Y, Sasaki A, Shibuya H, Ueno N, Ikeda K, Watanabe K (2001) Dlxin-1, a novel protein that binds Dlx5 and regulates its transcriptional function. *J Biol Chem* **276:** 5331–5338

McKinnell IW, Rudnicki MA (2004) Molecular mechanisms of muscle atrophy. *Cell* **119:** 907–910

Medina R, Wing SS, Haas A, Goldberg AL (1991) Activation of the ubiquitin-ATP-dependent proteolytic system in skeletal muscle during fasting and denervation atrophy. *Biomed Biochim Acta* **50:** 347–356

Mitch WE, Goldberg AL (1996) Mechanisms of muscle wasting. The role of the ubiquitin-proteasome pathway. *N Engl J Med* **335:** 1897–1905

Mitch WE, Price SR (2001) Transcription factors and muscle cachexia: is there a therapeutic target? *Lancet* **357:** 734–735

Natsume T, Yamauchi Y, Nakayama H, Shinkawa T, Yanagida M, Takahashi N, Isobe T (2002) A direct nanoflow liquid chromatography-tandem mass spectrometry system for interaction proteomics. *Anal Chem* **74:** 4725–4733

Opipari Jr AW, Boguski MS, Dixit VM (1990) The A20 cDNA induced by tumor necrosis factor alpha encodes a novel type of zinc finger protein. *J Biol Chem* **265:** 14705–14708

Pickart CM, Cohen RE (2004) Proteasomes and their kin: proteases in the machine age. *Nat Rev Mol Cell Biol* **5:** 177–187

Price SR, Bailey JL, Wang X, Jurkovitz C, England BK, Ding X, Phillips LS, Mitch WE (1996) Muscle wasting in insulinopenic rats results from activation of the ATP-dependent, ubiquitin-proteasome proteolytic pathway by a mechanism including gene transcription. *J Clin Invest* **98:** 1703–1708

Richly H, Rape M, Braun S, Rumpf S, Hoege C, Jentsch S (2005) A series of ubiquitin binding factors connects CDC48/p97 to substrate multiubiquitylation and proteasomal targeting. *Cell* **120:** 73–84

Ross CA, Poirier MA (2004) Protein aggregation and neurodegenerative disease. *Nat Med* **10** (Suppl): S10–S17

Sacheck JM, Ohtsuka A, McLary SC, Goldberg AL (2004) IGF-I stimulates muscle growth by suppressing protein breakdown and expression of atrophy-related ubiquitin ligases, atrogin-1 and MuRF1. *Am J Physiol Endocrinol Metab* **287:** E591–E601

Saeki Y, Saitoh A, Toh-e A, Yokosawa H (2002) Ubiquitin-like proteins and Rpn10 play cooperative roles in ubiquitin-dependent proteolysis. *Biochem Biophys Res Commun* **293:** 986–992

Sandri M, Sandri C, Gilbert A, Skurk C, Calabria E, Picard A, Walsh K, Schiaffino S, Lecker SH, Goldberg AL (2004) Foxo transcription factors induce the atrophy-related ubiquitin ligase atrogin-1 and cause skeletal muscle atrophy. *Cell* **117:** 399–412

Scott DA, Greinwald Jr JH, Marietta JR, Drury S, Swiderski RE, Vinas A, DeAngelis MM, Carmi R, Ramesh A, Kraft ML, Elbedour K, Skworak AB, Friedman RA, Srikumari Srisailapathy CR, Verhoeven K, Van Gamp G, Lovett M, Deininger PL, Batzer MA, Morton CC, Keats BJ, Smith RJ, Sheffield VC (1998) Identification and mutation analysis of a cochlear-expressed, zinc finger

protein gene at the DFNB7/11 and dn hearing-loss loci on human chromosome 9q and mouse chromosome 19. *Gene* **215:** 461–469

Seigneurin-Berny D, Verdel A, Curtet S, Lemercier C, Garin J, Rousseaux S, Khochbin S (2001) Identification of components of the murine histone deacetylase 6 complex: link between acetylation and ubiquitination signaling pathways. *Mol Cell Biol* **21:** 8035–8044

Stitt TN, Drujan D, Clarke BA, Panaro F, Timofeyva Y, Kline WO, Gonzalez M, Yancopoulos GD, Glass DJ (2004) The IGF-1/PI3K/Akt pathway prevents expression of muscle atrophy-induced ubiquitin ligases by inhibiting FOXO transcription factors. *Mol Cell* **14:** 395–403

Tawa Jr NE, Odessey R, Goldberg AL (1997) Inhibitors of the proteasome reduce the accelerated proteolysis in atrophying rat skeletal muscles. *J Clin Invest* **100:** 197–203

Thrower JS, Hoffman L, Rechsteiner M, Pickart CM (2000) Recognition of the polyubiquitin proteolytic signal. *EMBO J* **19:** 94–102

Verma R, Oania R, Graumann J, Deshaies RJ (2004) Multiubiquitin chain receptors define a layer of substrate selectivity in the ubiquitin-proteasome system. *Cell* **118:** 99–110

Wertz IE, O'Rourke KM, Zhou H, Eby M, Aravind L, Seshagiri S, Wu P, Wiesmann C, Baker R, Boone DL, Ma A, Koonin EV, Dixit VM (2004) De-ubiquitination and ubiquitin ligase domains of A20 downregulate NF-kappaB signalling. *Nature* **430:** 694–699

Wilkinson CR, Ferrell K, Penney M, Wallace M, Dubiel W, Gordon C (2000) Analysis of a gene encoding Rpn10 of the fission yeast proteasome reveals that the polyubiquitin-binding site of this subunit is essential when Rpn12/Mts3 activity is compromised. *J Biol Chem* **275:** 15182–15192

Wing SS, Goldberg AL (1993) Glucocorticoids activate the ATP-ubiquitin-dependent proteolytic system in skeletal muscle during fasting. *Am J Physiol* **264:** E668–E676

Wing SS, Haas AL, Goldberg AL (1995) Increase in ubiquitin-protein conjugates concomitant with the increase in proteolysis in rat skeletal muscle during starvation and atrophy denervation. *Biochem J* **307** (Part 3): 639–645

Young P, Deveraux Q, Beal RE, Pickart CM, Rechsteiner M (1998) Characterization of two polyubiquitin binding sites in the 26 S protease subunit 5a. *J Biol Chem* **273:** 5461–5467

Zambrowicz BP, Friedrich GA, Buxton EC, Lilleberg SL, Person C, Sands AT (1998) Disruption and sequence identification of 2000 genes in mouse embryonic stem cells. *Nature* **392:** 608–611

JOURNAL OF BONE AND MINERAL RESEARCH
Volume 20, Number 10, 2005
Published online on June 20, 2005; doi: 10.1359/JBMR.050610

Multi-Detector Row CT Imaging of Vertebral Microstructure for Evaluation of Fracture Risk

Masako Ito,[1] Kyoji Ikeda,[2] Masahiko Nishiguchi,[3] Hiroyuki Shindo,[4] Masataka Uetani,[1] Takayuki Hosoi,[5] and Hajime Orimo[6]

ABSTRACT: We applied MDCT for in vivo evaluation of the microarchitecture of human vertebrae. Microstructure parameters, such as structure model index, Euler's number, and bone volume fraction, revealed higher relative risk for prevalent vertebral fracture than did BMD obtained by DXA. Thus, microstructure analysis by MDCT, together with simultaneously obtained volumetric BMD values, is useful for clinical assessment of fracture risk.

Introduction: BMD measurement by DXA alone has limitations in predicting fracture, and methods for clinical assessment of bone quality, such as microstructure, are awaited. This study was undertaken to examine the applicability of multidetector row CT (MDCT) for in vivo evaluation of trabecular microstructure.
Materials and Methods: Optimal conditions for MDCT scanning were determined at a spatial resolution of 250 × 250 × 500 μm, using μCT data of excised human vertebra specimens as a reference. We analyzed the trabecular microstructure of the vertebrae of 82 postmenopausal women (55–76 years old), including 39 women with and 43 without a recent vertebral fracture.
Results: Microstructure indices obtained by MDCT scanning revealed higher relative risk for prevalent vertebral fracture (OR: 16.0 for structure model index, 13.6 for bone volume fraction, and 13.1 for Euler's number) than did spinal BMD obtained by DXA (OR: 4.8). MDCT could also provide volumetric BMD data, which had higher diagnostic value (OR: 12.7) than did DXA.
Conclusion: Vertebral microarchitecture can be visualized by MDCT, and microstructure parameters obtained by MDCT, together with volumetric BMD, provided better diagnostic performance for assessing fracture risk than DXA measurement.
J Bone Miner Res 2005;20:1828–1836. Published online on June 20, 2005; doi: 10.1359/JBMR.050610

Key words: osteoporosis, fracture, CT, microstructure

INTRODUCTION

BMD MEASUREMENTS ARE widely used for the diagnosis of osteoporosis and for the evaluation of the efficacy of treatment for this disease. However, BMD measurements alone have limitations in predicting fracture. In fact, a recent study indicates that 82% of postmenopausal women with fracture had BMD measurements in the osteopenic, not osteoporotic, range.[1] In addition, there is accumulating evidence that only a small fraction of the reduction in fracture with therapy can be accounted for by the increase in BMD.[2] These results suggest that factors other than BMD, such as bone structure and turnover rate of bone remodeling, contribute to bone fragility.[3]

μCT enables us to evaluate, at an ultra-high resolution, the microstructure of bone samples without destroying them, but it cannot be used in vivo. Studies by high-resolution CT, using different texture analysis methods as well as thresholding techniques, have reported results on its use.[4–6] However, the in-plane spatial resolution of conventional high-resolution CT is only 400 × 400 μm, and this conventional CT only gives information on the characteristic texture of a structure, such as rough versus smooth, homogeneous versus heterogeneous, or high versus low orientation of trabecular distribution. The reason for this is that the trabecular structure is subjected to partial-volume effects. Spiral CT has a higher resolution than conventional CT; however, it is subjected to scan-axis partial volume effects. Multidetector row CT (MDCT) is a new technique that has a substantially higher spatial resolution than standard spiral CT (i.e., it provides an in-plane spatial resolution of 250 μm and a minimum slice thickness of 500 μm) and thus promises to improve the assessment of trabecular bone structure.

The authors have no conflict of interest.

[1]Department of Radiology, Nagasaki University School of Medicine, Nagasaki, Japan; [2]Department of Bone and Joint Disease, The Research Institute, National Center for Geriatrics and Gerontology, Obu, Aichi, Japan; [3]Department of Orthopedic Surgery, Japan Ekisai-kai Nagasaki Hospital, Nagasaki, Japan; [4]Department of Orthopedic Surgery, Nagasaki University School of Medicine, Nagasaki, Japan; [5]Department of Internal Medicine, Tokyo Metropolitan Institute of Gerontology and Geriatric Hospital, Tokyo, Japan; [6]Health Science University, Tokyo, Japan.

This study was undertaken to apply MDCT for 3D imaging of the trabecular microarchitecture of human vertebrae and to evaluate the use of the microstructure parameters obtained by MDCT for the assessment of fracture risk in postmenopausal women.

MATERIALS AND METHODS

Specimen study

Specimens: Five formalin-fixed specimens of vertebrae of female cadavers (62–83 years of age at the time of death) were obtained from Tokyo Metropolitan Institute of Gerontology and Geriatrics Hospital. These vertebrae were used to define the appropriate scanning milli-ampere second value within clinically available values that revealed trabecular microstructure with a low signal-to-noise ratio. To compare the MDCT images with those obtained by μCT, we mounted the excised vertebral specimens on a sample holder of 40 mm diameter filled with an 8% gelatinous solution containing 88% protein, 1% mineral, and 11% water to keep the specimens steady. Specimens that contained air on CT images were excluded. The study protocol was approved by the ethical committee of Tokyo Metropolitan Institute of Gerontology and Geriatrics.

Imaging by μCT: μCT scanning was performed ex vivo on excised human vertebrae to validate MDCT images and data. A μCT apparatus (μCT40) and its analysis software were purchased from SCANCO Medical (Basserdorf, Switzerland).[7] Details of an earlier model (μCT20) were described previously.[8] The process was piloted by an Alpha DS10 workstation (Compaq Computer Corp.), and an open VMS system in a cluster configuration was used to perform 3D analysis. Each specimen was positioned as so to permit scanning of 600 slices with 40-μm increments with a spatial resolution of ~40 μm.

Imaging by MDCT: After μCT scanning, bone specimens in the holder were placed in a 20-cm thickness water-equivalent solid phantom (Standard Grade Solid Water Gammex 457; GAMMEX RMI) and scanned by MDCT. Axial CT images with a collimation of 0.5 mm, a table feed of 2 mm, and a reconstruction index of 0.3 mm were obtained with a MDCT system having four detectors (SOMATOM plus 4 Volume Zoom; Siemens, Erlangen, Germany). An ultra-high spatial resolution kernel was applied (head, filter H 70 very sharp). CT scanning of excised vertebra was performed with the following scanning conditions: field of view (FOV) of 100 mm and pixel matrix of 512 × 512, leading to a maximal spatial resolution of ~250 × 250 × 500 μm^3.

We first determined optimal conditions for MDCT scanning by using excised human vertebrae and compared the MDCT data with those obtained by μCT as a reference. Figure 1 shows images of an excised human vertebra obtained by μCT (Fig. 1A, with the volume of interest shown by a square), high-resolution CT images obtained by MDCT at 200, 250, and 300 mAs (Fig. 1B), their binarized images (Fig. 1C), and reconstructed 3D images (Fig. 1D). Scanning at 350 mAs was not performed because of overload of X-ray tube use for clinical cases. Measurements were repeated at the same position five times, and precision of repeated measurements was 2.35 ± 0.56% for bone volume/total volume (BV/TV), 2.21 ± 2.91% for trabecular number (Tb.N), 3,17 ± 3.28% for trabecular thickness (Tb.Th), 3.62 ± 1.29% for trabecular separation (Tb.Sp), 7.45 ± 1.26% for Euler's number, 4,08 ± 1.48% for structural model index (SMI), and 4.21 ± 1.42% for fractal dimension (n = 3 each).

Structure analysis: Both MDCT image data and μCT data were transferred to a workstation (Precision 360; Dell), and structural indices were calculated using a 3D image analysis system (TRI/3D-BON; RATOC System Engineering Co., Tokyo, Japan). To compare the parameters between μCT images and MDCT images, we defined the volume of interest (VOI) in μCT images first, and then adjusted it for MDCT images with reference to the VOI in μCT images. Grayscale images were segmented by using a median filter to remove noise with a fixed threshold to extract mineralized bone components. We used a standardized method of image thresholding based on the density histogram of a selected region of interest (ROI) to ensure consistency in the image thresholding across all subjects studied. Isolated small particles in the marrow space and isolated small holes in bone were removed by using a cluster-labeling algorithm.

Trabecular microstructure parameters were calculated in 3D as follows: bone volume (BV) was calculated using tetrahedrons corresponding to the enclosed volume of the triangulated surface. Total tissue volume (TV) was the entire volume of analysis, and apparent trabecular bone volume fraction (app BV/TV) was calculated from these values. Apparent trabecular thickness (app Tb.Th) was determined according to the method described by Hildebrand and Ruggsegger.[9] Apparent trabecular number (app Tb.N) and apparent trabecular separation (app Tb.Sp) were estimated based on the plate model.[10]

In addition to the computation of metric parameters, nonmetric parameters were calculated to obtain the 3D nature of the trabecular bone samples. Fractal dimensions of trabecular bone were measured as a representative of complexity using the box-counting method[11] that was developed in 3D. Connectivity was calculated by using the Euler method of Odgaard and Gundersen (Euler's number).[12] Degree of anisotropy (DA) was determined from the ratio between the maximal and minimal radii of the mean intercept length (MIL) ellipsoid.[13]

The interactive analysis time, including data examination, ROI definition, and image segmentation, was ~10 minutes for each type of data.

Biomechanical study

Specimens and microstructure analysis: Four femoral head specimens were obtained during surgery for femoral neck fracture at Nagasaki Rosai Hospital (2 men, 70 and 78 years of age; 2 women, 83 and 85 years of age). Surrounding soft tissues were removed, and 10-mm^3 specimens were prepared and stored at –20°C before use. The study protocol was approved by the ethical committee of Nagasaki Rosai Hospital.

These specimens were placed in an acrylic tank containing physiological saline solution and scanned by MDCT. Scanning direction was adjusted to the direction of loading

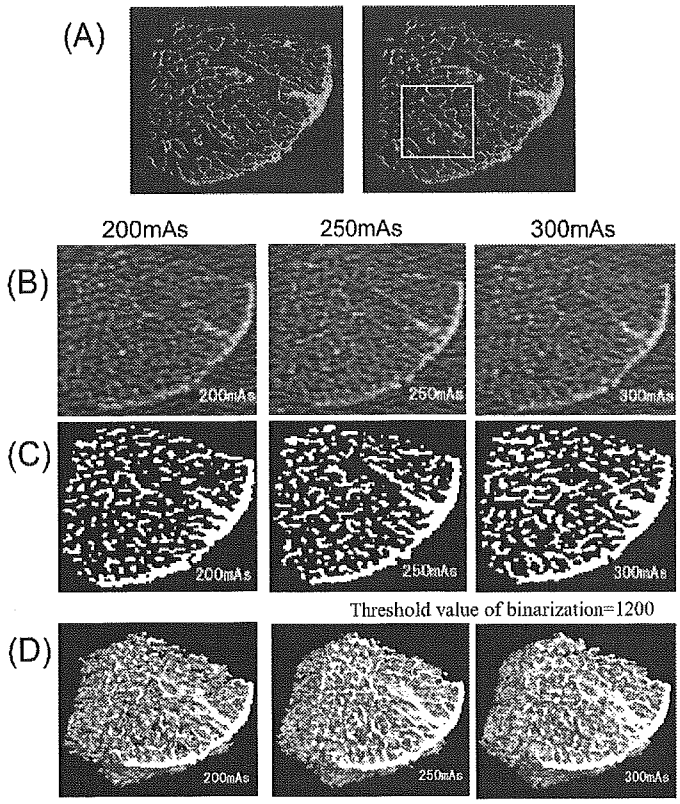

Threshold value	mAs	r	p
1120	200	0.656	ns
	250	0.487	ns
	300	0.959	< 0.01
1200	200	0.665	ns
	250	0.899	< 0.05
	300	0.979	< 0.005
1280	200	0.629	ns
	250	0.886	< 0.05
	300	0.959	< 0.05

FIG. 1. Visualization of spinal microstructure by MDCT scanning. Representative images of excised human vertebrae by (A) μCT image (volume of interest delimited by the square) and (B–D) MDCT images are shown. MDCT images were obtained under different conditions at 200, 250, and 300 mA; each CT image was analyzed at different threshold values (1120, 1200, and 1280). (B) Original 2D MDCT images at 200, 250, and 300 mA. (C) Binarized 2D CT images at 200, 250, and 300 mAs. (D) 3D CT images at 200, 250, and 300 mAs. The binarized and 3D images were prepared by using a threshold value of 1200. The linear correlations (r) and statistical significances (p) between apparent BV/TV measured by μCT and MDCT at 200, 250, and 300 mAs are also shown at the right.

in the biomechanical test. The scanning condition was the same as in the cadaver specimen study described above. Microstructure parameters were obtained for all of the specimens by the same procedure described above.

Determination of bone strength by compression test: Specimens were placed centrally on the compression testing fixture, which is able to hold the specimen stably in the cylinder and load only compressive direction without rotation or bending, and was attached to the materials-testing machine (Instron model 5582). A compression force was applied in a cranio-caudal direction using the fixture at a nominal deformation rate of 0.5 mm/minute and a sampling rate of 20 Hz. Crosshead displacement was recorded as specimen deformation. A load-deformation curve was displayed with a monitoring recorder linked to the tester in each specimen. The ultimate load (kgf) was obtained directly from the load-deformation curve.

Patient study

Patients: Spinal microarchitecture was examined in 82 postmenopausal women (55–76 years old, 65.3 ± 4.8 years) with MDCT scanning. Microstructure parameters were compared between 39 women who experienced their first spinal fracture during the previous 6 months (age: 66.2 ± 3.8 years old) and 43 women without fracture (age: 64.4 ± 5.5 years old) to assess the correlation between these parameters and fracture. Spinal fracture was defined according to the criteria proposed by Genant et al.[14] (i.e., vertebral deformity was considered as a fracture when at least a 20% reduction in anterior, middle, and/or posterior height and a 10% reduction in area were observed). Individuals who had had an osteoporotic fracture 6 months or more before the study were excluded, because bone structure would have been altered by the fracture. None of the postmenopausal women had received drugs affecting bone mass or bone metabolism within 6 months before the study. Nagasaki University ethics committee approved the protocol, and all subjects (i.e., fracture cases and controls) gave their informed consent.

BMD measurements: BMD of the lumbar spine (L_2–L_4) in antero-posterior (AP) projection was determined using DXA, and fractured vertebrae were excluded from the analysis. The obtained values were expressed as units of grams per centimeter squared for the projected area. Expert-EL (Lunar Corp., Madison, WI, USA) was used to measure the BMD of the lumbar spine. The CV (short-term precision) for L_2–L_4 was 1.1%.

To obtain volumetric BMD data by QCT, we scanned the patients simultaneously with MDCT using a bone mineral reference phantom (B-MAS2000; KYOTOKAGAKU Co.,

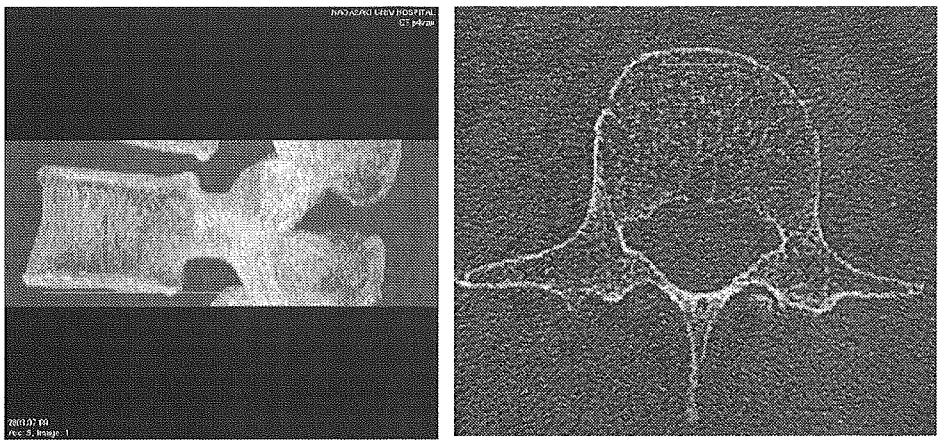

(A) (B)

FIG. 2. ROI for analysis of trabecular microstructure by MDCT. (A) The whole third lumbar spine including both endplates was scanned by MDCT. (B) The volume of interest (VOI) of 65 × 65 pixels in plane was defined in the anterior part of the spongiosa (delimited by the square) to avoid cortex and the basivertebral foramen.

Kyoto, Japan) containing calibration objects with equivalent densities of 0, 50, 100, 150, and 200 mg/cm^3 calcium hydroxyapatite. Reconstructed stacked 3D volume data of the vertebral body with reference phantom were used for the determination of volumetric BMD. VOI was defined in the same region for microstructure measurement of the reconstructed vertebral CT image.

Imaging by MDCT and structure analysis: The whole third lumbar spine including both endplates was scanned by MDCT, as shown in Fig. 2A. Patients were in the supine position for horizontal scanning of the vertebral body. The vertebral body was scanned under the appropriate X-ray condition, which was determined in the ex vivo cadaver study as described above. For the analysis of microstructure, the size of the VOI of 65 × 65 pixels in plane was defined (Fig. 2B); the total number of slices varied according to the size of the vertebral body. The VOI was defined manually within the internal part of the cancellous bone to avoid the cortex, the basivertebral foramen, and both endplates. The midline of the VOI in the x-axis in the axial image was in the center of the vertebral body, and the frontal edge on both sides of the VOI was just behind the cortex. The average number of slices was 43.8 ± 5.3 (range, 28–52 slices).

The procedure for structure analysis was the same as that for the cadaver specimen study described above. Samples from three patients were scanned five times on different days, using manually defined VOI; the precision was confirmed by the same operator. Precision of measurements of microstructure parameters was 0.67% for fractal dimension, 0.84% for Tb.Th, 1.13% for SMI, 2.04% for DA, 6.57% for Tb.N, 7.13% for BV/TV, 7.36% for Tb.Sp, and 12.30% for Euler's number.

Statistical analysis

Data analysis was performed with the software statistical package for Social Science, SPSS (SPSS, Chicago, IL, USA). Mean and SD of microstructure parameters and BMD were calculated for the postmenopausal women with or without fracture. The significance of differences between the two groups was calculated by ANOVA and posthoc test (Fisher's protected least significant difference [PLSD]), at the 95% significance level. Correlations of microstructure parameters or BMD with age or body weight of the subjects and correlations between microstructure parameters and BMD were assessed using linear regression analysis. Area under the curve (AUC) in receiver operator characteristic (ROC) analysis was generated to determine the diagnostic efficacy for detection of fracture cases. Additionally, the ORs per SD were calculated by logistic regression analysis to provide an estimate for the discriminatory capability of each variable for spinal fracture, as a single parameter or in combination with DXA or QCT value.

RESULTS

Specimen study

Optimal conditions for MDCT scanning: To determine the optimal conditions for MDCT scanning, we obtained vertebral specimens from cadavers and scanned them by both μCT (Fig. 1A) and MDCT (Figs. 1B–1D). Microstructure parameters were calculated at threshold values of 1120, 1200, and 1280 to binarize bone CT images. These values of threshold were numbers on a scale from 0 to 4290 according to linear attenuation, which has no units. As shown in Fig. 1 (right), at all three threshold levels, BV/TV obtained by μCT revealed the highest correlation with app BV/TV by MDCT at 300 mAs (r = 0.979, $p < 0.005$ at a threshold value of 1200).

When scanned at 0.5 mm thickness, 71-mm scan length, 0.8 feed/rotation, and 120 kVp, weighted CT dose indices (CTDIw) were 46.3 mGy for 200 mAs, 59.1 mGy for 250 mAs, and 77.1 mGy for 300 mAs.

Correlation between microstructure parameters and biomechanical properties: To examine whether microstructure parameters correlate with biomechanical properties, another set of four specimens were obtained from the femoral head at surgery and subjected to compression test after scanning by μCT and MDCT. As shown in Fig. 3, microstructure parameters obtained by MDCT revealed a high correlation with ultimate load (kgf); a significant correlation with the ultimate load was obtained for app BV/TV ($p < 0.05$), SMI ($p < 0.05$), and app Th.N ($p < 0.05$).

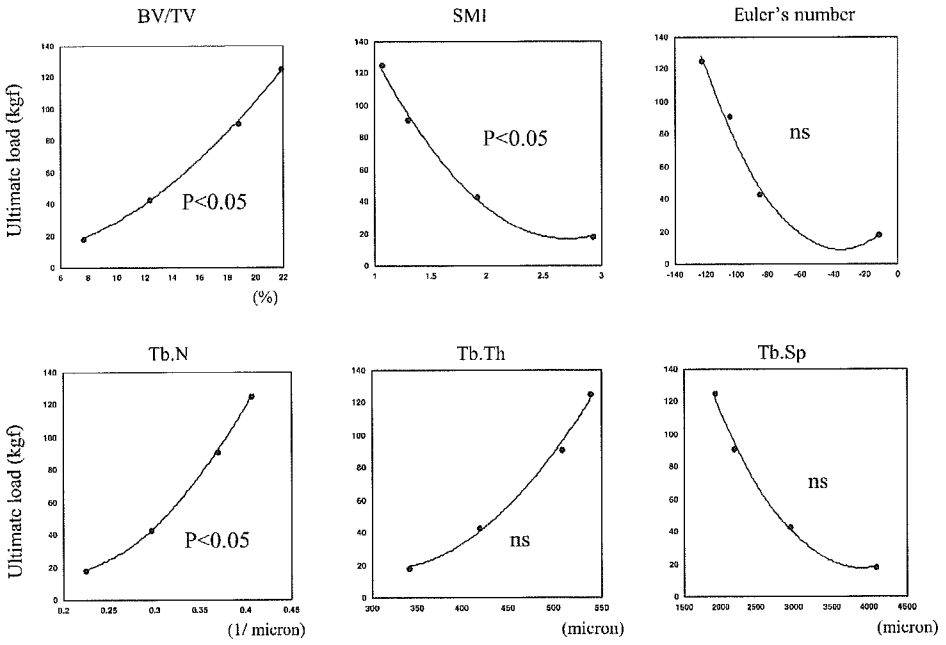

FIG. 3. Correlation between microstructure parameters and bone strength. Ten-millimeter cubic specimens were obtained from the femoral head of four individuals and scanned by μCT and MDCT. Structure analysis was performed as described in the Materials and Methods section. The specimens were subjected to biomechanical test, and the ultimate load was obtained from the load-deformation curve. Shown are significant correlations between microstructure parameters obtained by MDCT and bone strength. p values are shown for each parameter.

Patient study

Association of microstructure parameters with prevalent spinal fracture: To examine the use of trabecular microarchitecture information obtained by MDCT scanning for the assessment of fracture, we compared the microstructure parameters derived from MDCT images between 43 women without fracture (age: 64.4 ± 5.5 years old) and 39 women with a recent spinal fracture (age: 66.2 ± 3.8 years old). As shown in Table 1, there was no significant difference in age, age at menopause, body height (BH), or body weight (BW) between these two groups of women.

Figures 4A–4F show representative 2D (Figs. 4A and 4B), its binarized 2D (Figs. 4C and 4D), and 3D (Figs. 4E and 4F) MDCT images of the third lumbar vertebra of a 62-year-old woman without vertebral fracture (Figs. 4A, 4C, and 4E) and those of a women of the same age with a fracture in the thoracic spine (Figs. 4B, 4D, and 4F).

Table 1 summarizes the results of microstructure parameters, as well as areal (by DXA) and volumetric (by MDCT) BMD values in the two groups of women. Areal BMD by DXA was significantly lower in postmenopausal women with a fracture than in those without one (0.836 ± 0.191 versus 0.925 ± 0.161 g/cm^2, $p < 0.05$). Among the microstructure indices obtained by MDCT, app BV/TV, app Tb.N, app Tb.Th, and fractal dimension were significantly lower; whereas app Tb.Sp, SMI, Euler's number, and DA were significantly higher in women with a fracture than in those without a fracture (Table 1). Volumetric BMD determined by MDCT was also significantly lower in postmenopausal women with a fracture (72.0 ± 18.5 versus 103.9 ± 23.5 mg/cm^3, $p < 0.0001$).

Table 2 shows the correlation of microstructure parameters with BMD values obtained by DXA and QCT. Most microstructure parameters were more highly correlated with volumetric BMD by QCT than with areal BMD by DXA.

ROC analysis was performed to determine the diagnostic value of microstructure parameters with respect to fracture (Table 3). The highest AUC value was obtained for SMI (0.928), which was significantly higher than that for areal BMD by DXA (0.647) or volumetric BMD by MDCT (0.870). AUC values of Euler's number (0.857) and app Tb.Sp (0.818) were similar to that value of volumetric BMD, and significantly exceeded that of areal BMD by DXA. The ORs for the association of SMI (16.0), app BV/TV (13.6), Euler's number (13.1), app Tb.Sp (7.4), fractal dimension (7.4), app Tb.N (6.6), and app Tb.Th (5.5) with fracture were higher than the OR for that of areal BMD by DXA with it (4.8); the ORs for SMI, app BV/TV, and Euler's number exceeded that ratio of volumetric BMD (12.7). Multivariate regression analysis showed significant correlations of SMI (R^2 = 0.329, $p < 0.0001$) and Tb.Th (R^2 = 0.154, $p < 0.005$), as well as volumetric BMD (R^2 = 0.159, $p < 0.005$), with fracture (Table 4). Combining areal or volumetric BMD data with some microstructural parameters further increased R^2 values compared with BMD alone (Table 4).

Table 5 shows the correlations of spinal microarchitecture or BMD with age and BW. Most microstructure parameters and volumetric BMD by MDCT correlated with age, especially SMI, Euler's number, and app BV/TV, whereas areal BMD values by DXA showed a moderate correlation with both age and BW.

DISCUSSION

The purpose of this study was to evaluate the diagnostic value of in vivo analysis of spinal trabecular microstructure, focusing on its association with prevalent spinal fracture. Compared with postmenopausal women without a spinal fracture, those with one had a smaller trabecular bone fraction (app BV/TV: 36.1 versus 26.2) in association with fewer